Future Cities and Environment
ISSN 2363-9075 Volume 12 (2026)

https://doi.org/10.70917/fce-2026-007
Article

Ultimate Bending Capacity of Wind Turbine Tower Structures: A New Empirical Formulation Based on the Geometric and Material Factors

Raden Althaaf Ulwandaffa Dhaneswara [1,2], Alfido Marchandi Faizatama [1,2], Hensa Akbar Al Kautsar [1,2], Ristiyanto Adiputra [3,*], Aditya Rio Prabowo [1,*], Sören Ehlers [4,5], Moritz Braun [4], Bambang Kusharjanta [1] and Eko Prasetya Budiana [1]

[1] Department of Mechanical Engineering, Universitas Sebelas Maret, Surakarta 57126, Indonesia
[2] Laboratory of Design and Computational Mechanics, Faculty of Engineering, Universitas Sebelas Maret, Surakarta 57126, Indonesia
[3] Research Center for Hydrodynamics Technology, National Research and Innovation Agency (BRIN), Surabaya 60117, Indonesia
[4] Institute for Maritime Energy Systems, German Aerospace Center (DLR), Geesthacht 21502, Germany
[5] Institute for Ship Structural Design and Analysis, Hamburg University of Technology, Hamburg 21073, Germany
* Corresponding authors: ristiyanto.adiputra@brin.go.id (R.A.); aditya@ft.uns.ac.id (A.R.P.)

Abstract: Wind energy is emerging as the most promising sustainable energy source due to its abundant resources and environmental benefits. One of the most essential parts of a wind turbine system is the tower, as it is responsible for supporting the weight of the tower top and the loads given by its environment. The preliminary design of the tower section of the wind turbine system is crucial to ensure the system's safety, and a simplified formula is needed to make it more practical. A comprehensive series of ultimate strength analyses on tapered pipes was performed to optimize the tower design, involving the variation and cross-combination of numerous geometric and material parameters. A total of 900 tapered pipe configurations were assessed using finite element method (FEM) analysis via the ABAQUS/CAE program. In the case of tapered cylindrical shells length variations, there was an increase in bending moment from the plastic deformation phase to the critical phase of 29%, 31%, and 39% for pipes measuring 50 m, 30 m, and 10 m, respectively, with the highest ultimate moment of 278.7 kN·m achieved at a pipe length of 50 m. The ultimate bending moment values were then formulated through regression analysis, resulting in a derived formula to predict the ultimate bending capacity of tapered pipes for wind turbine structures. The findings revealed that varying multiple parameters significantly impacted the ultimate strength and critical failure modes of the tapered pipe. The newly developed formula showed good accuracy, providing a reliable tool for design predictions.

Keywords: Tapered tower pipe; Ultimate strength; Bending moment; Non-linear regression; Derived formula

Highlights:

- FEM analysis on a 900-tapered pipe model under pure bending load.
- Analysis of the effect of the geometric and material factors on a tapered pipe under pure bending load.
- Regression analysis of the tapered pipe's ultimate moment to produce a forecasting formula.
- The validation of the derived formula shows an error margin below 10%
- The newly derived formula has proven to be an efficient tool for simplifying the wind tower design process.

1. Introduction

World demand for energy has consistently surged on a global scale for the last decade due to rapid urbanization and economic development (Liu et al., 2017; Faizatama et al., 2025a). Several options exist

to fulfill the increasing need for energy, but some come at an environmental cost (Patil et al., 2023). Burning fossil fuels for energy production is a significant contributor to environmental pollution, exacerbating the already devastating effects of global warming. Moreover, the depletion of fossil fuel reserves, such as coal and oil, is also becoming a significant problem in meeting the worldwide energy demand. With the United Nations' target to achieve net zero emissions by 2050, many countries began to increase their interest in the adoption of renewable energies as a potential solution to these issues (Ahmed et al., 2024; Mandal & Reddy, 2025; Zhang et al., 2025). Carbon emissions created to produce energy using renewable energy are very small (Prabowoputra et al., 2020; Prasetyo et al., 2022; Shame et al., 2025; Zhang et al., 2025). With that in mind, renewable energy, such as wind energy, is considered to be one of the promising renewable energy options (Michael et al., 2021; Ren et al., 2022; Adiputra et al., 2023; Fauzi et al., 2024; Wijaya et al., 2025; Budisetyawan et al. 2025; Faizatama et al., 2025b).

Wind energy is considered one of the most promising forms of renewable energy due to its abundance, sustainability, and low environmental impact (Al Kautsar et al., 2024). Wind power harnesses natural wind patterns to generate electricity without emitting greenhouse gases or consuming finite resources. It is a vital solution for combating climate change and reducing reliance on fossil fuels. Wind energy can be harvested from two sources, onshore and offshore systems, as depicted in Figure 1. Onshore wind systems, located on land, are generally more accessible and less expensive to install and maintain, making them a popular choice for many regions. However, offshore wind systems situated in bodies of water offer significant advantages due to more robust and consistent wind speeds, leading to higher energy yield. These offshore systems can generate more power and are ideal for countries with limited land space, as the availability of surface area in the ocean is higher, which means a more significant potential for installation (Dvorak et al., 2010; Yanez-Rosales et al., 2024). Both systems can make a significant contribution to the global transition towards cleaner energy.

(a) (b)

Figure 1. Wind Turbine Systems: (a) Onshore systems; (b) Offshore systems (Rehling et al., 2023; Sun et al., 2012)**.**

Wind energy is site-specific based on its capacity, as the site on which the system is situated can affect the wind strength. A typical wind turbine system can be broken down into three main components: the rotor, nacelle, and tower (Hernandez-Estrada et al., 2021). The wind tower itself is an integral part of the structure, which is used to support the weight of the tower top and the loads generated by the force of the wind and its environmental conditions (Xu et al., 2021).

Figure 2. Wind turbine failure due to high wind speed (Chen et al., 2015; Yu & Amdahl, 2023)**.**

As an integral component of a wind turbine system, the tower structural design is the structural design

of the tower is a crucial concern in the development process. Wind turbine towers are prone to failure without an adequate design capable of withstanding environmental effects such as high wind speeds, as shown in Figure 2. For this reason, the preliminary design of the tower section is critical to ensuring the system's safety and stability in energy generation. During the design stage of the wind tower, a formula is required to simplify the process and prevent the tower from buckling.

Studies have been proposed on the formulation to optimize cylindrical shells used for wind towers. Fajuyigbe and Brennan (2022) proposed a formulation to calculate the limit bending moment of cracked cylindrical shells used for offshore wind turbine monopiles. Yang et al. (2022) proposed extrapolation methods and empirical formula for estimating wind loads in wind towers under varying wind speeds. Huang et al. (2022) proposed a geometric optimization of a hybrid wind tower design using a genetic algorithm. Several others have formulated the formula for the ultimate strength of curved panels used in wind tower construction. Kim et al. (2014) studied the fundamental buckling and collapse behaviors of cylindrically curved plates under varying loads to formulate a simple formula using regression. Park et al. (2018) investigated the cylindrically curved plate under axial compression and lateral load to create a formula to predict the ultimate strength derived from Faulkner's formula. Kim et al. (2024) proposed an empirical formulation to predict the ultimate limit state of curved plates under compression. Despite the fact that earlier studies have proposed empirical formulations, extrapolation methods and geometric optimisation approaches for analysing the ultimate strength of cylindrical shells and curved panels in wind towers, no research has specifically addressed the ultimate bending capacity of tapered cylindrical shells or tapered pipes. This highlights a significant research gap in the provision of pragmatic design formulations for tapered wind turbine towers.

This study makes a novel contribution by explicitly investigating the coupled influence of taper ratio and shell slenderness on the ultimate bending capacity of tapered wind turbine towers, an area that has not been addressed in previous research. In order to achieve this objective, a broad and feasible design space was curated to represent realistic tower configurations, incorporating variations in both geometry and material properties that reflect practical design considerations. Within this space, a comprehensive finite element dataset comprising 900 models was generated using ABAQUS/CAE, systematically constructed by varying and cross-combining tower length, length-to-bottom diameter ratio, upper-to-bottom diameter ratio, bottom diameter-to-thickness ratio, and yield stress level. Each model was subjected to bending loads in order to capture the ultimate bending response. This enabled the distribution pattern of bending capacity to be mapped across the full design space. This offers insights beyond those obtained from simplified cylindrical or panel-based studies. The numerical dataset was then analysed using regression techniques to establish a compact empirical relation expressed entirely in terms of geometric ratios. This relation captures the coupled influence of taper and slenderness. It also provides a simplified yet reliable means of predicting ultimate bending capacity without reliance on exhaustive simulations. The derived relation was then verified against the finite element database to determine its accuracy and applicability limits, ensuring its value as a practical tool for preliminary design while simultaneously bridging the gap between detailed numerical simulations and design-oriented formulations for tapered wind turbine towers.

2. Literature Review

The behavior of cylindrical shells under bending load can be governed by a set of equations derived from previous study. These equations describe the relationship between stresses, strains, and deformations, considering the geometry and material properties of the shell structure. The governing equations are described in the following sections.

2.1. Nonlinear Kinematics of Cylindrical Shells

According to a study by (Som & Deb, 2014), nonlinear buckling of thin cylindrical shells involves the analysis of kinematics and complex stress relationships. The main strains under prebuckling conditions are formulated as Equation (1).

$$\varepsilon_{x0} = u_{0,x} + \frac{1}{2}w_{0,x}^2 \; ; \; \varepsilon_{y0} = \frac{w_0}{a} + \frac{1}{2}w_{0,y}^2 \; ; \; \gamma_{xy0} = \left(v_{0,x} + u_{0,y} \right) + \; w_{0,x}w_{0,y} \tag{1}$$

These strains relate the displacements u_0, v_0, and w_0 to the geometric parameters of the shell under prebuckling conditions. For the perturbation condition, the strains are formulated by considering both linear and nonlinear contributions as Equation (2).

$$\begin{aligned} \varepsilon_{x1} = u_{1,x} + w_{0,x}w_{1,x} \; ; \; \varepsilon_{y1} = v_{1,y} + \frac{w_1}{a}w_{0,y}w_{1,y} \; ; \; \gamma_{xy1} \\ = \left(v_{1,x} + u_{1,y} \right) + \; w_{0,x}w_{1,y} + w_{0,y}w_{1,x} \end{aligned} \tag{2}$$

This strain takes into account the interaction between prebuckling deformation (w_0) and perturbation (w_1). The curvature (K) of the shell is represented by the relationship Equation (3).

$$K_{xi} = -w_{i,xx}\ ;\ K_{yi} = -w_{i,yy}\ ;\ K_{xyi} = -w_{i,xy} \tag{3}$$

This relationship describes the local geometry variation of the shell due to deformation. The constitutive relationship for membrane stress is given by Equation (4).

$$N_{xi} = C(\varepsilon_{xi} + v\varepsilon_{yi});\ N_{yi} = C(\varepsilon_{yi} + v\varepsilon_{xi});\ N_{xyi} = C\left(\frac{1-v}{2}\right)\gamma_{yxi} \tag{4}$$

The parameter C is the elastic modulus of the membrane, which depends on Poisson's ratio (v). For the bending moment, the constitutive relationship is expressed as Equation (5).

$$\begin{gathered} M_{xi} = D(K_{xi} + vK_{yi});\ M_{yi} = D(K_{yi} + vK_{xi}); \\ M_{xyi} = D(1-v)K_{xyi};\ Q_{xi} = M_{xi,x} + M_{xyi,y} \end{gathered} \tag{5}$$

The solution for the prebuckling radial deformation W_0 follows Equation (6).

$$W_0 = 2av\gamma\bar{N}[1 + A_1 \sin\left(\frac{\xi_1 x}{a}\right)\sin.\,\mathrm{h}\left(\frac{\xi_2 x}{a}\right) + A_2 \cos\left(\frac{\xi_1 x}{a}\right)\cos.\,\mathrm{h}\left(\frac{\xi_2 x}{a}\right) \tag{6}$$

These parameters include constants A_1 and A_2 calculated through boundary conditions, as well as geometry and material parameters. The kinematic relations (Eqs. 1 - 6) establish the fundamental strain–curvature expressions that serve as the local geometric basis in the FEM formulation. Subsequently, these models are reformulated within the framework of the finite element method (FEM) to account for the geometric non-uniformity of tapered shells.

2.2. Theoretical Strength Estimation for Cylindrical Shells in Bending

The primary deformation characteristic of a cylindrical shell subjected to bending is ovalization, whereby the initially circular cross-section progressively flattens into an oval shape. This phenomenon, known as the Brazier effect, significantly reduces bending stiffness and governs the onset of collapse. For long shells with restrained ends, Timoshenko and Gere (1985) demonstrated that the corresponding critical stress, (σ_{CR}), can be determined from Equation (7). The following strength estimations (Eqs. 7 - 9) describe the elastic limit conditions of thin cylindrical shells, providing analytical references for evaluating how taper-induced stiffness variations influence the elastic response in the present study.

$$\sigma_{CR} = \frac{Et}{r\sqrt{3(1-v^2)}} \tag{7}$$

For thin-walled pipes subjected to a bending moment load, the maximum stress can be calculated using Equation (8) (Polenta et al., 2015).

$$M_y = \pi r^2 t \sigma_y \tag{8}$$

In the case of a thin-walled pipe experiencing buckle bending load, the moment it reaches the critical point can be determined by integrating Equations (4 and 5). Assuming the material is steel with a Poisson's ratio of 0.3, the critical moment can be found using Equation (9) (Adie et al., 2023).

$$M_{CR} = \sigma_{CR}\pi r^2 t = 0.605\pi E r^2 t \tag{9}$$

Previous studies on pipes under bending loads, as conducted by Brazier (1927), Chwalla (1933), revealed that their findings spanned a range of values between 0.55 and 1.3 times the values derived from Equation (9).

The previous equations can be used to estimate the critical moment, but they are insufficient to calculate the actual critical moment of a circular pipe. This is because the critical moment is also influenced by other factors, especially the ratio of the pipe's diameter to its thickness, which plays a vital role in determining the essential moment, a critical geometric consideration. Despite being derived for prismatic shells, (Eqs. 7 - 9) remain valuable as reference benchmarks for interpreting the FEM responses of tapered shells.

2.3. Bending Moment of Cylindrical Shells

The plastic moment relations (Eqs. 10 - 11) define the classical full-plastic capacity of thin-walled cylindrical shells, originally derived for ideal elastic–plastic materials under small-displacement assumptions. These formulations, based on the work of (Sadowski & Rotter, 2013), establish benchmark conditions for validating the FEM-derived plastic capacity of tapered shells. In the context of the present study, they serve to bridge the transition from idealized prismatic behavior to geometrically non-uniform configurations.

$$M_p = \frac{4}{3}\sigma_y \left[\left(r + \frac{t}{2}\right)^3 - \left(r - \frac{t}{2}\right)^3\right] \tag{10}$$

This equation is derived from the analysis of tube cross-sections considering an even distribution of plastic stresses across the cross-section when the maximum bending moment is reached. The model assumes small deformations, where the deformation of the tube is considered not to change the geometry of the cross section significantly. These equations form the basis for understanding the limits of a tube's ability to withstand bending loads before undergoing permanent and significant plastic deformation. Accordingly, the use of M_p as a dependent variable in the regression model is well justified.

The study by (Mork et al., 1997) also modeled the bending moment as Equation (11).

$$M_p = \left[1.05 - 0.0015\frac{D}{t}\right]\sigma_y D^2 t \tag{11}$$

2.4. Reference Resistance Design

The Reference Resistance Design (RRD) framework provides a unified analytical approach for evaluating the elastic–plastic resistance of cylindrical shells under bending This is based on the study of (Wang et al., 2020), which presents the RRD framework developed by Rotter (2016a,b). the framework defines two reference moments $R_{pl} = M_{pl}$ and $R_{cr} = M_{cr}$ representing the plastic and elastic buckling limits, respectively. Neglecting length effects, these resistances can be expressed through small-displacement formulations (Eqs. 12 - 13). Within this study, the RRD concept is employed as a theoretical benchmark to interpret how taper-induced geometric nonuniformity modifies the transition between elastic, inelastic, and plastic regimes.

$$M_{pl} = \left(4r^2 t + \frac{1}{3}t^3\right)\sigma_y \approx 4r^2 t\sigma_y \; as \; \frac{r}{t} \to \infty \tag{12}$$

$$M_{cr} = \frac{\pi}{\sqrt{3(1-v^2)}} Ert^2 \tag{13}$$

Where σ_y is the yield stress, E is the modulus of elasticity, and v is Poisson's ratio. The RRD framework is based on the basic relationship between the characteristic failure resistance of a system (χ) and the dimensionless ramping (λ), illustrated by Rotter (2005;2007). The most proper form of the capacity curve function is shown in Equation (14) (Feliciano et al., 2018; Rotter, 2011).

$$\chi(\lambda) = \begin{cases} \chi_h - \left(\frac{\lambda}{\lambda_0}\right)(\chi_h - 1) \;\rightarrow\; \lambda \le \lambda_0 \; (plastic) \rightarrow where \; \chi = \frac{R_k(\lambda)}{R_{pl}} \\ 1 - \beta\left(\frac{\lambda - \lambda_0}{\lambda_p - \lambda_0}\right)^{\eta(\lambda)} \rightarrow \lambda_0 < \lambda < \lambda_p \; (el.plas) \rightarrow \eta(\lambda) = \eta_0\left(\frac{\lambda_p - \lambda}{\lambda_p - \lambda_0}\right) + \eta_p\left(\frac{\lambda - \lambda_0}{\lambda_p - \lambda_0}\right) \\ \frac{\alpha_G \alpha_I}{\lambda^2} \;\rightarrow\; \lambda_p \le \lambda \; (elastic) \rightarrow \; \lambda_p = \sqrt{\frac{\alpha_G \alpha_I}{1-\beta}} \; and \; \lambda = \sqrt{\frac{R_{pl}}{R_{cr}}} \end{cases} \tag{14}$$

The elastic reduction factor ($\alpha_G \alpha_I$) accounts for geometric nonlinearity and imperfection sensitivity, with α_I for a perfect shell. The plastic span factor (β) determines the onset of inelastic influence for slender below λ_p, which limits Class 3 noncompact and Class 4 slender, while λ_0 indicates the full plastic moment (M_{pl}) at the boundary between Class 2 compact and Class 3 noncompact.

Resistance can be described in four behavioral domains, differentiated by cylinder length and expressed in dimensionless form, as shown in Equation (15) (Rotter et al., 2014). The RRD framework is employed as a reference tool not directly implemented in the regression but it serves to guide the interpretation of elastic - plastic transition zones observed numerically.

$$\omega = \frac{L}{\sqrt{rt}} \; and \; \Omega = \frac{L}{r}\sqrt{\frac{t}{r}} \tag{15}$$

2.5. Transversely-Isotropic Elastic Under Bending

Initial Stability and Ovalization. The buckling phenomenon in elastic cylinders subjected to bending can be understood through the critical longitudinal stress condition that occurs at the ovalization section of the cylinder. Based on Donnell's buckling theory for cylindrical shells (Brush et al., 1975), buckling conditions occur when the longitudinal stress around the cylinder reaches a critical value, such as Equation (16).

$$\sigma_x = \frac{E}{\sqrt{3(1-\nu^2)}}\left(\frac{t}{r_{\theta 0}}\right) \tag{16}$$

These equations relate the material properties (E and ν) with the geometric parameters of the cylinder (t and $r_{\theta 0}$) to determine when buckling occurs. Cylinders with small thickness or large radius have lower critical stress values, thus are more prone to buckling (Brazier, 1927). In addition, the critical buckling wavelength is given by Equation (17).

$$L_{hw}^{axi} = \frac{\pi\sqrt{r_{\theta 0}t}}{[12(1-\nu^2)]^{1/4}} \tag{17}$$

where L_{hw}^{axi} is the buckling half-wavelength. This wavelength depends on the local radius rh, thickness t, and Poisson's ratio ν. This equation shows that the longitudinal buckling pattern has sinusoidal characteristics, with a wavelength that depends on a combination of material properties and cylinder geometry (Stephens et al., 1975).

Deformation Tensor and Virtual Working Principle. In the stability analysis of the elastic cylinder, the material deformation is defined using the deformation velocity tensor (d_{kl}), which is the symmetric part of the velocity gradient as shown in Equation (18).

$$d_{kl} = \frac{1}{2}\left(V_{m/l}(\boldsymbol{G}^m \cdot \boldsymbol{g}_k) + V_{m/k}(\boldsymbol{G}^m \cdot \boldsymbol{g}_l)\right) \tag{18}$$

where $V_{m/l}$ is the covariant derivative of the velocity vector component with respect to the reference basis, $\boldsymbol{G}^m$ is the covariant basis vector in the reference configuration, $\boldsymbol{g}_k$ is the covariant basis vector in the deformed configuration. This equation describes how deformation is represented through the change in relative velocity between the covariant basis in the initial and deformed configurations.

Virtual Work Principle. Mechanical equilibrium is expressed through the virtual work principle, which states that the internal work due to the variation of virtual displacement must be equal to the external work, which is mathematically written in Equation (19).

$$\int_{V_0} \delta U_{i/j}\,(\boldsymbol{G}^i \cdot \boldsymbol{g}_k)\tau^{kj} dV_0 = \int_B \delta \boldsymbol{U} \cdot \boldsymbol{t} dB_q + M\delta\theta \tag{19}$$

where $\delta U_{i/j}$ is the virtual displacement variation, τ^{kj} is the Kirchhoff stress tensor, $\boldsymbol{t}$ is the surface force, M is the bending moment, $\delta\theta$ is the rotation angle variation of the cylinder tip. The virtual displacement variation $\delta U_{i/j}$ is described as Equation (20).

$$\delta U_{i/j} = \frac{\partial(\delta \boldsymbol{u})}{\partial \xi^j}\boldsymbol{G}_i \tag{20}$$

Constitutive Relationship. In the context of hypoelasticity, the constitutive relationship between the Kirchhoff stress tensor ($\dot{\tau}^{ij}$) and the deformation velocity tensor is given as Equation (21), with $\Re^{ijkl}$ as the instantaneous modulus tensor.

$$\dot{\tau}^{ij} = \Re^{ijkl} d_{kl} \tag{21}$$

Alternatively, for hyperelastic materials, the relationship between the second Piola-Kirchhoff tensor ($\boldsymbol{S}$) and the Kirchhoff tensor ($\boldsymbol{\tau}$) is expressed as Equation (22), where $\boldsymbol{F}$ is the deformation gradient.

$$\boldsymbol{\tau} = \boldsymbol{F}\boldsymbol{S}\boldsymbol{F}^T \tag{22}$$

The component τ^{ij} in the deformed configuration can be expressed as Equation (23). Assuming convected coordinates Equation (24) applies.

$$\tau^{ij}(\boldsymbol{g}_i \otimes \boldsymbol{g}_j) = \boldsymbol{F}\left[S^{ij}(\boldsymbol{G}_i \otimes \boldsymbol{G}_j)\right]\boldsymbol{F}^T \tag{23}$$

$$\tau^{ij} = S^{ij} \tag{24}$$

The virtual working principle can be rewritten with the second Piola-Kirchhoff tensor as Equation

(25).

$$\int_{V_0} \delta U_{k/j} (\boldsymbol{G}^k \cdot \boldsymbol{g}_i) S^{ij} dV_0 = \int_B \delta \boldsymbol{U} \cdot \boldsymbol{t} dB_q + M\delta\theta \tag{25}$$

The relationship between the Lagrange-Green strain tensor and the second Piola-Kirchhoff tensor (S) is formulated as Equation (26). with D^{ijkl} as the fourth-order stiffness tensor.

$$S^{ij} = D^{ijkl} E_{kl} \tag{26}$$

The time derivative of this relationship is Equation (27), From continuum mechanics is given as Equation (28), which in covariance coordinates yields Equation (29).

$$\dot{\boldsymbol{E}} = \boldsymbol{F}^T \boldsymbol{dF} \tag{27}$$

$$\dot{E}_{ij} = d_{ij} \tag{28}$$

Representation of Deformation and Ovalization. In the numerical model of an anisotropic cylinder, the deformation of the deformed configuration is described in a finite element formulation based on longitudinal and circular discretization. The position of a point in the deformed configuration is expressed as a combination of translational and rotational displacement at the node, as well as local deformation. The formulation is given as Equation (30).

$$\boldsymbol{X}(\theta, \zeta, \rho) = \sum_{k=1}^{3} \left[\left(\boldsymbol{X}^{(k)} + \boldsymbol{r}^{(k)}(\theta) + \rho \boldsymbol{n}^{(k)}(\theta) + \rho\gamma(\theta) \boldsymbol{e}_z^{(k)} \right) N^{(k)}(\zeta) \right] \tag{29}$$

where $\boldsymbol{X}^{(k)}$ is the (k)-th node position, $\boldsymbol{r}^{(k)}$ is the cross-section reference position, $\boldsymbol{n}^{(k)}(\theta)$ is the in-plane normal displacement. The interpolation function $N^{(k)}(\zeta)$ is used to numerically represent the circular displacement.

To describe ovalization and other deformations in the circular direction, the displacement functions $w(h)$, v(h), $u(h)$, and $c(h)$ are described in Fourier series. The radial displacement function $w(h)$ is given by Equation (31).

$$w(h) = a_0 + a_1 sin \cdot h + \sum_{n=2,4,6,\ldots} a_n cos \cdot nh + \sum_{n=3,5,7\ldots} a_n sin \cdot nh \tag{30}$$

While the longitudinal displacement $v(h)$ is formulated as Equation (32).

$$v(h) = -a_1 cos \cdot h + \sum_{n=2,4,6,\ldots} b_n sin \cdot nh + \sum_{n=3,5,7\ldots} b_n cos \cdot nh \tag{31}$$

$u(h)$ tangential displacement that represents ovality is shown in Equation (33).

$$u(h) = \sum_{n=2,4,6,\ldots} c_n cos \cdot nh + \sum_{n=3,5,7\ldots} c_n sin \cdot nh \tag{32}$$

and the out-of-plane rotational deformation $c(h)$ is given by Equation (34).

$$c(h) = \sum_{n=0,2,4,6,\ldots} c_n cos \cdot nh + \sum_{n=1,3,5,7\ldots} c_n sin \cdot nh \tag{33}$$

This formulation incorporates the essential displacement components required to represent ovalization and warping in both circumferential and longitudinal directions. The transversely isotropic relations describe these deformation mechanisms; although a fully anisotropic model is not employed, the isotropic assumption adopted in this study sufficiently captures the fundamental bending–buckling interaction of non-prismatic (tapered) shells. Accordingly, these equations provide a conceptual bridge between detailed shell kinematics and the simplified regression-based representation developed in Section 4.

2.6. Strength Estimation for Perfect Cylinders in Global Bending

Based on Chen et al. (2023), the axial elastic buckling wavelength is one of the key parameters in evaluating the stability of thin cylindrical shells under axial compression. The following classical strength formulations (Eqs. 35 - 40) are summarised for prismatic cylinders and are used as theoretical benchmarks in validating and interpreting the derived regression formulation. These equations describe the elastic and plastic bending limits of idealised uniform shells. However, they do not explicitly account for stiffness gradients or geometric non-uniformity introduced by tapering. Consequently, they provide the analytical foundation for developing a generalised regression model capable of extending these classical relationships to tapered geometries. The elastic buckling wavelength can be calculated by

Equation (35).

$$\lambda_{cl} = \frac{\pi}{[12(1-v^2)]^{1/4}}\sqrt{rt} \cong 1.728\sqrt{rt} \tag{34}$$

This equation shows that the buckling wavelength depends on a combination of material characteristics and geometric dimensions, such as radius and thickness. Furthermore, the classical elastic buckling stress is used to determine the elastic limit of the material before plastic deformation occurs. This stress is expressed as Equation (36).

$$\sigma_{cl} = \frac{E}{\sqrt{3(1-v^2)}}\frac{t}{r} \cong 0.605\frac{Et}{r} \tag{35}$$

In this equation, the elastic modulus E, Poisson's ratio v, radius r, and thickness t affect the amount of buckling stress that can be achieved before the shell loses its elastic stability. For very long cylinders, the critical bending moment can be calculated using the minimum strain energy principle formulated by Brazier, such as Equation (37).

$$M_{Braz} = 0.987\left(\frac{E}{\sqrt{1-v^2}}\right)t^2 r \cong 1.035Et^2 r \tag{36}$$

This equation shows that the critical bending moment depends strongly on the elastic modulus of the material and geometric factors such as the radius and thickness of the cylinder. However, in medium-length cylinders, the effect of ovalization on the shell cross section is more controllable, so the critical bending moment can be calculated as Equation (38).

$$M_{cr} = \pi\left(\frac{E}{\sqrt{3(1-v^2)}}\right)t^2 r \cong 1.90Et^2 r \tag{37}$$

This equation applies to conditions where the stress distribution and deformation remain uniform throughout the cylindrical section. When the most compressed fiber reaches the yield stress, the bending moment that occurs is given by Equation (39).

$$M_y = \pi r^2 t\sigma_y \tag{38}$$

This equation reflects the direct relationship between the yield stress of the material (σ_y) and the geometric dimensions of the cylinder (r and t). Finally, when full plastic deformation is achieved throughout the cross-section, the full plastic bending moment can be expressed as Equation (40).

$$M_p = \frac{4}{3}\sigma_y\left[\left(r+\frac{t}{2}\right)^3 - \left(r-\frac{t}{2}\right)^3\right] \tag{39}$$

These equations account for the strain distribution of the material and the effect of thickness on the total bending capacity. Through the above set of equations, the mechanical behavior of thin cylindrical shells under global bending conditions can be theoretically analyzed. This approach provides a solid foundation for understanding various failure mechanisms that depend on the geometry and material properties of the shell. Nevertheless, these equations inherently apply to prismatic shells and do not capture taper-induced stiffness gradients, thereby motivating the regression model developed to generalize these relations for tapered geometries.

2.7. Milestone Study

Following the classical review presented in the previous section, this part summarises key analytical, numerical, and design-oriented studies on cylindrical and tapered shells to identify existing knowledge gaps related to tapered geometries. The literature on the ultimate strength of wind turbine towers further emphasises the importance of these structures within modern wind energy systems.

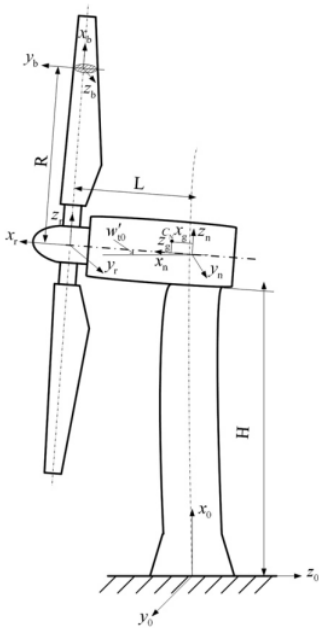

Figure 3. Various coordinate systems in wind turbine towers for analytical purposes (Wang et al., 2010).

Historically, research has been conducted both analytically (Feliciano et al., 2018; Hammad & Yu, 2024; Hegseth & Bachynski, 2019; Wang et al., 2010) as can be seen in Figure 3 and experimentally (Deng et al., 2023; Dimopoulos & Gantes, 2012; W. Ren et al., 2022) as can be seen in Figure 4. FEM has gained popularity in the analysis of wind turbine towers (Gentils et al., 2017; Hu et al., 2014; Sadowski, 2019), due to their ability to simulate structural behavior with high accuracy and precision, eliminating the need for complex manufacturing processes. This approach enhances the understanding of wind turbine tower behavior under various loading conditions related to environmental factors, facilitating a more effective preliminary design of the tower. Table 1 summarizes key developments in research on the ultimate strength of wind turbine towers under various loading conditions.

Several studies focus on enhancing the structural analysis and design of wind turbine towers and related structures by introducing advanced methods, such as thin-walled beam theory and hybrid beam-shell finite element models. These methods enhance the accuracy of stress, displacement, and failure predictions. Prior research highlights the importance of shell slenderness in buckling behavior and the need to account for geometric imperfections. Additionally, previous studies address the balance between reducing material costs through weight reduction and maintaining structural integrity, with recommendations to avoid resonance and ensure long-term turbine reliability.

Figure 4. Experimental testing of the pipe for the wind turbine tower under combined load (Deng et al., 2023).

Previous studies have demonstrated that shell tapering alters stiffness distribution and local buckling modes, leading to a reduction in bending strength by approximately 10–25% depending on the taper ratio (Hu et al., 2014). Further research has proposed optimization frameworks combining Finite Element Analysis (FEA) and Genetic Algorithms (GA) to achieve more efficient and reliable support structure designs compared with conventional methods. Several investigations also highlight the need to incorporate realistic atmospheric and operational conditions in wind turbine tower models to improve displacement and stability predictions. Additionally, innovations such as stiffened steel tubes, enhanced methods for evaluating the strength of tapered columns, and advanced frameworks for dynamic response analysis under extreme loading have contributed to improved design standards and overall structural performance.

In summary, previous analytical, code-based, and FEM/empirical studies do not explicitly capture the coupled influence of taper ratio and shell slenderness on ultimate bending capacity across practical spans. This lacuna in the literature is the central motivation for the present study. While past research has predominantly focused on cylindrical shells or curved panels, tapered geometries introduce additional complexities such as variable stiffness distribution, non-uniform stress paths, and interaction effects between axial compression and lateral bending. These characteristics fundamentally alter the local curvature and sectional rigidity along the tower height, leading to nonlinear bending responses that cannot be represented by formulations derived for uniform cylinders. Conventional models typically assume constant radius and stiffness, which result in inaccurate estimations of stress concentration and failure initiation points in tapered configurations. Therefore, a new formulation is required to quantify the bending strength of tapered towers more accurately.

To address this gap, the present study adopts a comprehensive finite element framework to systematically evaluate the ultimate bending capacity of tapered cylindrical shells. A large-scale parametric study encompassing 900 models was conducted to quantify the influence of taper ratio, diameter-to-thickness ratio, and shell slenderness. By integrating validated FEM simulations with regression-based analysis, we derive an empirical design equation that explicitly incorporates taper effects. This methodological framework, outlined in the next section, provides a reproducible and rigorous foundation for practical preliminary design formulations. All governing equations presented (Eqs. 1 - 40) are intentionally retained to ensure theoretical continuity with the regression development in Section 4. These relations collectively provide the analytic foundation required to generalise bending capacity for tapered cylindrical shells.

Table 1. Remarks on the pioneer works in wind turbine towers.

Year	Researcher(s)	Title	Subject	Remarks
2010	Wang et al. (2010)	Dynamic analysis of horizontal axis wind turbine by thin-walled beam theory	Development of a mathematical model to predict the dynamic performance of wind turbine systems.	The study addresses limitations in existing methods while providing detailed insights into the responses of flexible components, which previous models overlooked. The incorporation of thin-walled beam theory enhances the accuracy of stress and displacement calculations compared to previous parameter models.
2012	Dimopoulos and Gantes (2012)	Experimental investigation of buckling of wind turbine tower cylindrical shells with opening and	Buckling behavior of cantilevered shells with openings and stiffening, specifically on the geometric	The study highlights the importance of shell slenderness in buckling behavior and found a strong correlation between experimental results and numerical predictions for

		stiffening under bending	characteristics of wind turbine towers.	load-displacement curves and ultimate loads. However, strain measurements did not fully match due to the impact of geometric imperfections on buckling behavior.
2014	Hu et al. (2014)	Effect of internal stiffening rings and wall thickness on the structural response of steel wind turbine towers	the structural response and optimization of steel tubular wind turbine towers.	The study emphasizes the need to balance weight reduction with structural integrity. While reducing wall thickness cuts material costs, it increases horizontal sway and von Mises stress. The researchers recommend avoiding resonance at varying tower heights to ensure the longevity and reliability of wind turbines. It also emphasizes the importance of considering both static and dynamic behavior in design to optimize performance and minimize costs.
2017	Gentils et al. (2017)	Integrated structural optimisation of offshore wind turbine support structures based on finite element analysis and genetic algorithm	Structural optimization of offshore wind turbine support structures by integrating FEA and GA to optimize component designs.	The optimized geometry from the integrated approach is more advanced than the initial design, indicating improved structural efficiency and potential for enhanced performance. Integrating FEA and GA introduces a novel approach that simultaneously optimizes all support structure components, resulting in more effective designs than traditional single-component methods.
2018	Feliciano et al. (2018)	Generalized analytical displacement model for wind turbine towers under aerodynamic loading	Structural response of wind turbine towers under varying atmospheric conditions.	The study emphasizes the need to integrate realistic atmospheric conditions into structural analyses of wind turbines, as the wind turbines experience different tower displacements and deflections depending on atmospheric stratification

				and turbulence. The newly developed generalized analytical model demonstrates strong agreement with detailed numerical simulations, enabling the effective estimation of tower displacements based on inflow velocity and simplifying preliminary design stages.
2019	Hegseth and Bachynski (2019)	A semi-analytical frequency domain model for efficient design evaluation of spar floating wind turbines	Development of a semi-analytical frequency domain model for the efficient design evaluation of spar floating wind turbines.	The semi-analytical frequency approach significantly improves computational efficiency compared to fully coupled nonlinear time-domain simulations. The paper also emphasizes the importance of accounting for the tower's elasticity and structural dynamics in the design of floating wind turbines and their mooring systems.
2019	Sadowski (2019)	On the advantages of hybrid beam-shell structural finite element models for the efficient analysis of metal wind turbine support towers	Efficient analysis of metal wind turbine support towers using hybrid finite element models.	The hybrid beam-shell finite element model enhances the efficiency and accuracy of structural analyses by realistically estimating failure conditions in selected strakes. This approach provides valuable insights into the criticality of all strakes in a tower structure, helping identify weak points and optimize tower thickness under various load cases.
2022	Ren et al. (2022)	Experimental and analytical investigation of stiffened steel tubes for wind turbine towers under compression-bending load	Evaluating the effects of stiffeners to enhance steel tubes' ultimate strength and ductility.	The study demonstrates that the use of stiffened steel tubes in wind turbine towers significantly enhances structural stability and resistance to local buckling. It also recommends updating design standards to account for stiffened steel tubes, as current methods

				often overestimate the strength of unstiffened tubes while neglecting the advantages of stiffeners.
2023	Deng et al. (2023)	Coupled behaviour and strength prediction of tapered CFDST columns with large hollow ratios for wind turbine towers	Evaluating the performance of TLHR-CFDST columns under complex combined loads	TLHR-CFDST columns reduce weight and material costs due to their tapered design and high hollow ratios. The study presents a method for predicting the ultimate strength of these materials under combined loads, highlighting that current methods often overestimate strength, particularly for moderate or small bending-to-torsion ratios. It also examines how axial compressive ratio, tapered angle, hollow ratio, and height-to-diameter ratio affect load-deformation and ultimate characteristics of the columns.
2024	Hammad and Yu (2024)	A semi-analytical approach for dynamic responses of monopile-supported offshore wind turbines subjected to accidental loads	Design and analysis of offshore wind turbines (OWTs) that must withstand extreme and accidental loads, such as ship collisions and slamming waves.	The study presents a novel semi-analytical framework for evaluating the dynamic responses of monopile-supported OWTs subjected to accidental loads. This approach enhances understanding of structural behavior under extreme conditions and aids in improving design standards for offshore wind energy infrastructure.

3. Methodology

3.1. Research Flowchart

The flowchart of the analysis for estimating the ultimate bending capacity of a steel tapered cylindrical shell is presented in Figure 5. The initial problem is formulated by referencing earlier literature studies and utilizing existing research findings. The material properties, interaction settings, boundary, and loading conditions were applied to each tapered cylindrical shell model. AISI 1018 is chosen as the material with varying yield stresses. The selected data was determined as the ultimate bending moment from the simulation results, which were then normalized.

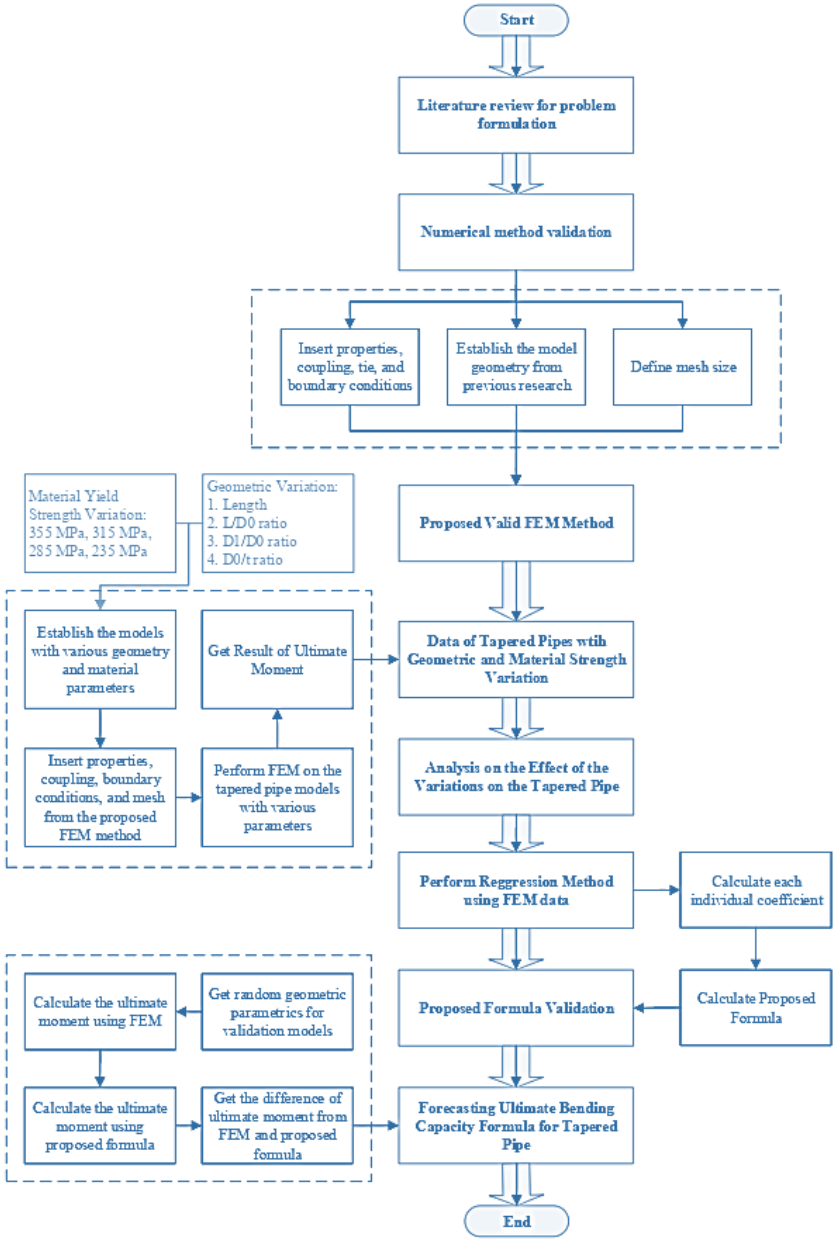

Figure 5. Finite element method flowchart.

The subsequent processing of the normalized data through a nonlinear regression method facilitates the determination of the correlation from all geometric parameters up to a specific order, thereby enabling the calculation of the coefficients' values. A comparison was then made between the ultimate bending capacity obtained from the derived formula and FEM simulations. The objective of this comparison was to ascertain whether the derived formula could predict the ultimate bending of tapered cylindrical shells. In addition, a detailed description of boundary conditions and material modeling has been provided to facilitate reproducibility and enable benchmarking by other researchers. This description remains directly relevant to the development and validation of the derived regression formula.

3.2. Finite Element Method

To validate the finite element method used in this research, validation is carried out by replicating the study conducted by Yadav and Gerasimidis (2019) on the steel cylindrical shell instability under bending load. This approach was employed because the numerical calculations were relatively straightforward and enabled efficient computations. The geometry used to validate this research is illustrated in Figure 6. The geometry used by Yadav and Gerasimidis (2019) is a cylindrical shell pipe with a length (L) of 20

meters, a diameter (D) of 4 meters, and a diameter/thickness ratio (D/t) of 120. The deployed material is medium carbon steel, characterized by a yield stress of 355 MPa, a Young's modulus of 210 GPa, and a Poisson's ratio of 0.3. The Ramberg-Osgood plasticity model is used for material input in ABAQUS/CAE. The result, which is the reaction moment, is then normalized by $M = D^2 t \sigma_y$. D is the pipe diameter, t is the thickness of the pipe, and σ_y is the yield stress.

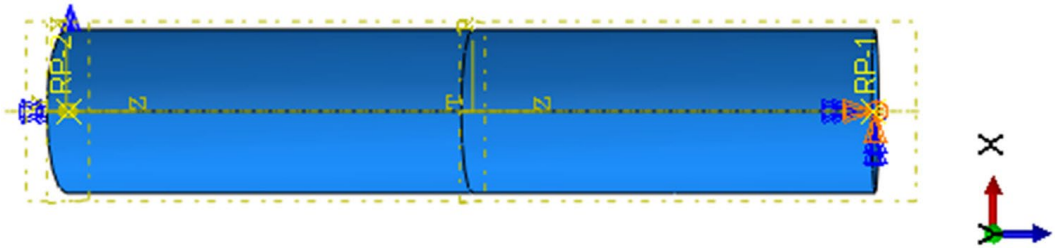

Figure 6. Boundary condition settings.

Table 2. Validation results.

Reference	Normalized Moment
Yadav and Gerasimidis (2019)	0.952
Present Research	0.994
Difference (%)	4.4

The boundary condition used also followed a study conducted by Yadav and Gerasimidis (2019). At the lower end of the pipe, there is no movement, so the ENCASTRE boundary condition ($U_1 = U_2 = U_3 = U_{R1} = U_{R2} = U_{R3} = 0$) is applied at the reference point at the bottom end. This boundary condition will restrict the pipe from moving in any direction, turning it into a clamped support. At the top end, the pipe can move on the x-axis, namely $U_1 = U_{R2} = U_{R3} = 0$. The material properties input into ABAQUS/CAE include Young's modulus, Poisson's ratio, yield stress, and the plasticity of the material used in the model. These properties can significantly impact the calculation of the ultimate moment for a cylindrical shell pipe subjected to bending loads, as described in Equations (3 and 4).

The results presented in Table 2 indicate that the ultimate moment difference between the research conducted by Yadav and Gerasimidis (2019) and the current study is similar. The difference in the normalized moment between the two research studies is less than 5%, specifically 4.4%. The mesh convergence study was also conducted using a replicated model from the study conducted by Yadav and Gerasimidis. The geometry, materials, and boundary conditions were identical to the previous validation. The elements used in this study were S4R shell elements (4-node doubly curved shell elements with reduced integration), which were selected because the geometry was a cylindrical shell, allowing for accurate and computationally efficient analysis. A full 3D model without symmetry assumptions was used to capture the global bending response under pure bending loads. The nonlinear solver was executed with standard convergence criteria, employing a force residual tolerance of 1×10^{-3} and a displacement increment tolerance of 1×10^{-4}, which ensured equilibrium convergence and stable numerical predictions.

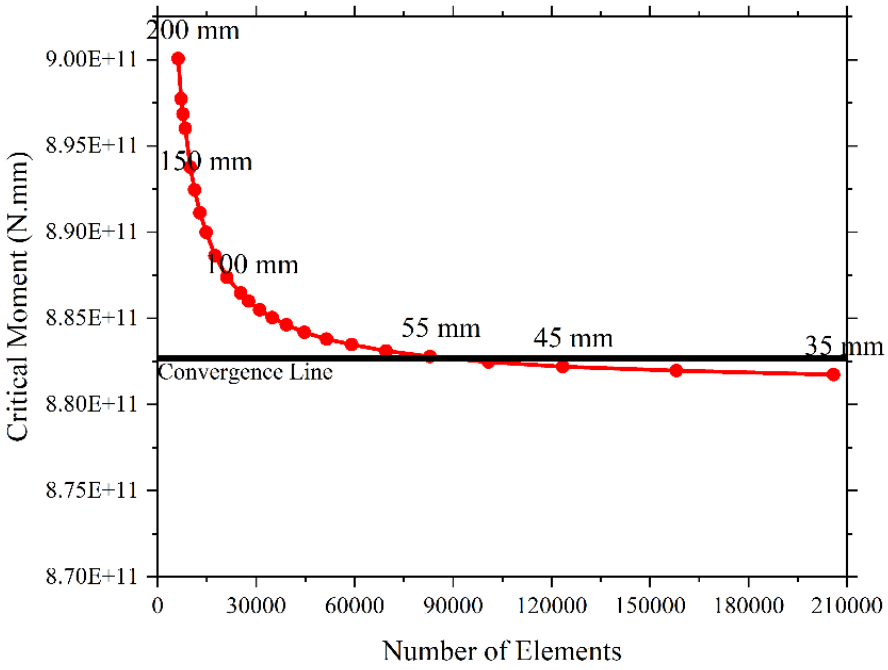

Figure 7. Mesh convergence results.

Figure 7 presents the mesh convergence study. For coarse meshes (200 mm, 150 mm, and 100 mm), the predicted critical moment fluctuated significantly because the limited number of elements could not adequately capture the curvature and stress gradients of the cylindrical shell. This produced an artificially stiffer response and overpredicted the ultimate capacity. Once the mesh size reached approximately 55 mm (corresponding to about 90,000 elements), the discretization became sufficiently refined to represent the stress distribution and buckling deformation pattern, and the results converged closely to the convergence line. Further refinement to 45 mm and 35 mm (up to 200,000 elements) produced no significant change in the critical moment, confirming that the ultimate bending capacity is insensitive to additional refinement beyond this point. Therefore, a mesh size of 55 mm was chosen as the optimal discretization, ensuring both accuracy and computational efficiency.

3.3. Case Configuration

The tapered shells are used according to their geometric variation, which is supported permanently below the wind turbine tower. Therefore, the boundary condition used is a cantilever under a bending load at the free end. The result that will be used is the residual speed, which is the maximum bending moment achieved by each model. The configuration of the tapered pipe used in this study is shown in Figure 8.

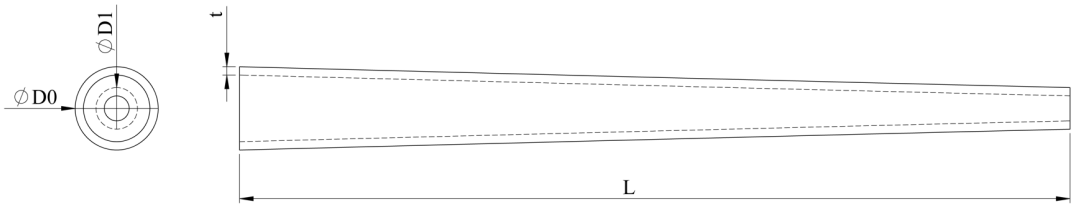

Figure 8. Case configuration.

Table 3 summarizes the geometric parameters used in this research. Nine hundred (900) different models with varying and cross-combining geometric parameters were chosen. Four geometric variations and a variation in material yield stresses were used in this research.

Table 3. Geometric parameters for numerical simulations.

L (m)	L/D_0	D_1/D_0	D_0/t	σ_y (MPa)
10	20	0.25	10	355
30	100	0.5	50	315
50	200	0.75	100	285
	300		150	235
	400		200	

3.4. Applied Materials

The material chosen in this research is the AISI 1080 steel. The material is picked as it is readily available on the market. The material chosen has varying yield stresses to determine the effect of different yield stresses on the tapered pipes. The Ramberg–the following Equation represents Osgood equation for plasticity (41) (Kyriakides et al., 2008). The Ramberg-Osgood equation is a cyclic material law that describes the material behavior under repeated loading. This equation can help predict how materials deform and fail when subjected to cyclic stresses. The material properties of AISI 1080 used in this study are presented in Table 4.

$$\varepsilon = \frac{\sigma}{E}\left[1 + \frac{3}{7}\left(\frac{\sigma}{\sigma_y}\right)^{n-1}\right] \tag{40}$$

Table 4. Material properties.

Material	Modulus Young	Yield Strength	Ultimate Strength	Density
AISI 1018 (Kyriakides et al., 2008)	210 GPa	355 MPa	455 MPa	7.840 kg/m^3

4. Result and Discussion

4.1. Effect of the tapered cylindrical shell variations

This section analyzes the effects of the applied variations on a tapered cylindrical shell structure subjected to bending loads. The variations under observation are bending moment, maximum stress, maximum strain, and maximum displacement for each sample. Only specific samples of the configuration case were considered in the FEM.

4.2. Length Variations

The results of this variation were compared using a graph of bending moment versus curvature. The selected model incorporates varying lengths while keeping the other parameters and material yield stresses identical. The models exhibited different ultimate strengths in relation to the length of the tapered cylindrical shell, as shown in Figure 9. The sample indicated that the ultimate bending moment rose as the pipe length increased. This occurred because an increase in pipe size typically leads to a rise in the moment of inertia, affecting the ultimate moment in bending scenarios. The formula for the moment of inertia of a hollow cylinder is provided in Equation (42) (Beer et al., 2021).

$$I = \frac{\pi}{64}(D^4 - d^4) \tag{41}$$

The graph in Figure 9 illustrates that the plastic deformation region was more significant in geometries with greater lengths than those with shorter ones. This occurs because the length of the geometry influences other geometric ratios, such as diameter and thickness, which can increase the area prone to plastic deformation.

The results of each modelling were visualized using stress contours with deformation scale factors applied to enlarge the displacements, with the sole purpose of improving clarity of the buckling mode shape. This scaling does not affect the quantitative stress or displacement values. Figure 10 displays the stress contours of tapered cylindrical shells with varying lengths (10 m, 30 m, and 50 m). In all cases, the regions of highest stress concentration are observed near the fixed end of the shell, indicating this as

the critical location for buckling initiation. While the overall stress distribution patterns are similar due to consistent material and geometric properties, longer shells exhibit a more gradual spread of stress along the height, whereas shorter shells concentrate stresses more locally at the base. This behavior explains why the 10 m model reached its ultimate moment earlier, while the 50 m model sustained higher loads before critical failure. The increase in bending moment from the plastic deformation phase to the critical phase for the 50 m, 30 m, and 10 m pipes is 29%, 31%, and 39%, respectively. The highest ultimate moment, 278.7 kN·m, was achieved with a pipe length of 50 m, as shown in Figure 9. This represents more than a threefold increase compared to the ultimate moment of the 30 m pipe and an extraordinary 131-fold increase compared to the 10 m pipe. This is due to the larger pipe's better thickness ratio, which enhances its resistance to buckling under load.

Figure 11 illustrates the strain contours of tapered cylindrical shells with different lengths (10 m, 30 m, and 50 m). In all models, strain localization is clearly observed at the base of the shell near the fixed end, consistent with the stress concentration patterns in Figure 11. The shorter shell (10 m) develops sharper strain gradients, indicating a more abrupt deformation response, while the longer shells (30 m and 50 m) display more distributed strain along the height. This distribution suggests that slender towers dissipate deformation more evenly, allowing them to sustain higher ultimate bending moments before failure. Figure 12 presents the displacement contours corresponding to the global buckling deformation of the tapered cylindrical shells. The 10 m model exhibits a localized curvature near the fixed base, characteristic of short-shell buckling behavior. By contrast, the 30 m and 50 m models show smoother and more gradual bending shapes along the shell height, reflecting the increased flexibility and energy dissipation capacity of longer towers. These displacement patterns explain the higher load-carrying capacity observed in longer shells and reinforce the role of slenderness in governing global stability.

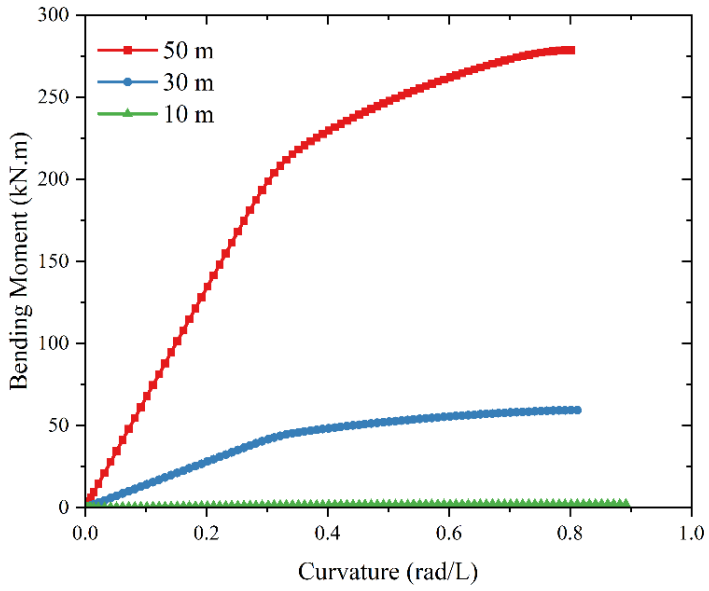

Figure 9. Moment-curvature graph for the length (L) variation.

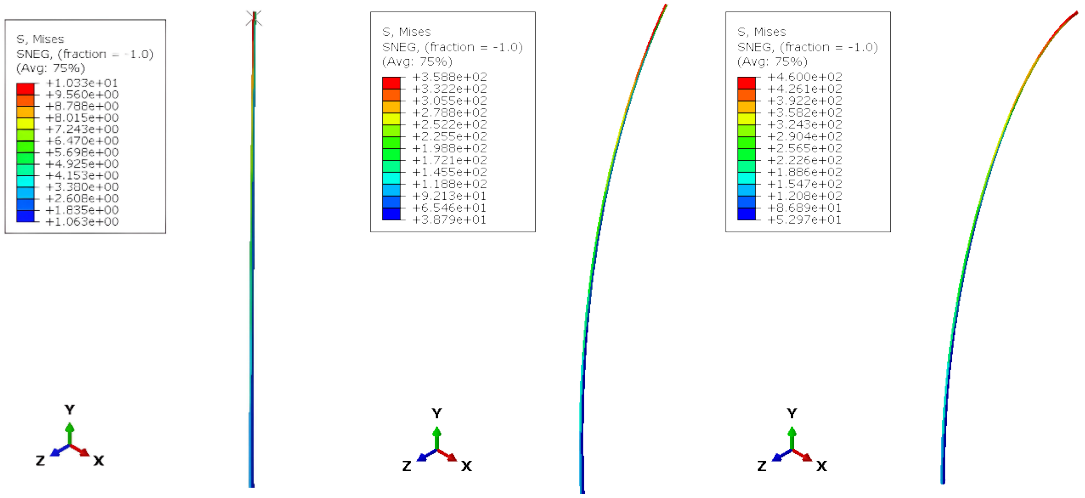

Scale factor = 2 (a)

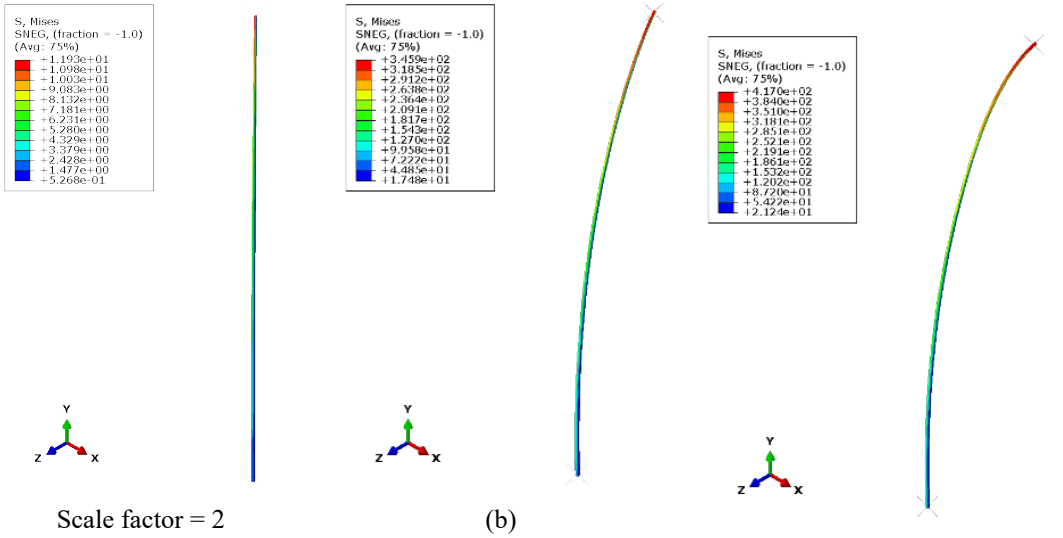

Scale factor = 2 (b)

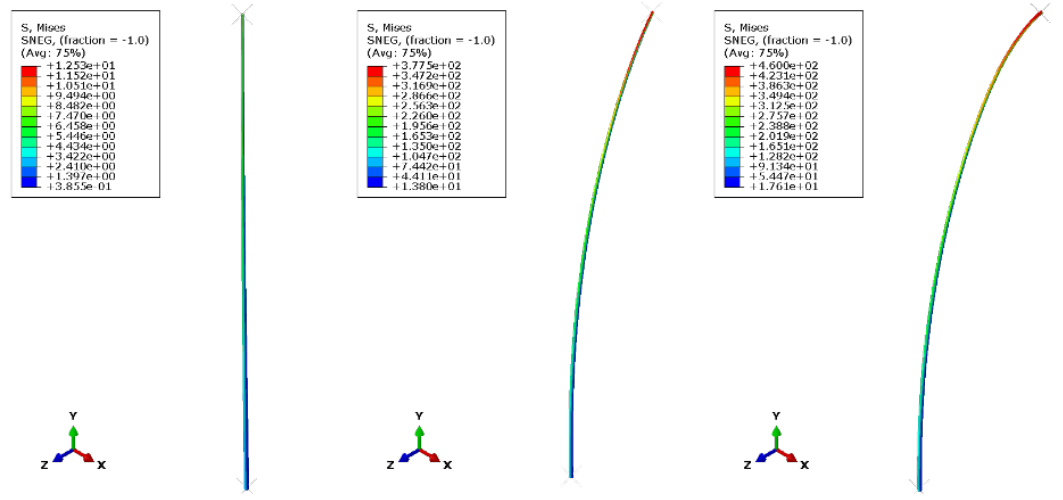

Scale factor = 2 (c)

Figure 10. Stress contours of tapered cylindrical shells with different lengths: (a) 10 m, (b) 30 m, and (c) 50 m.

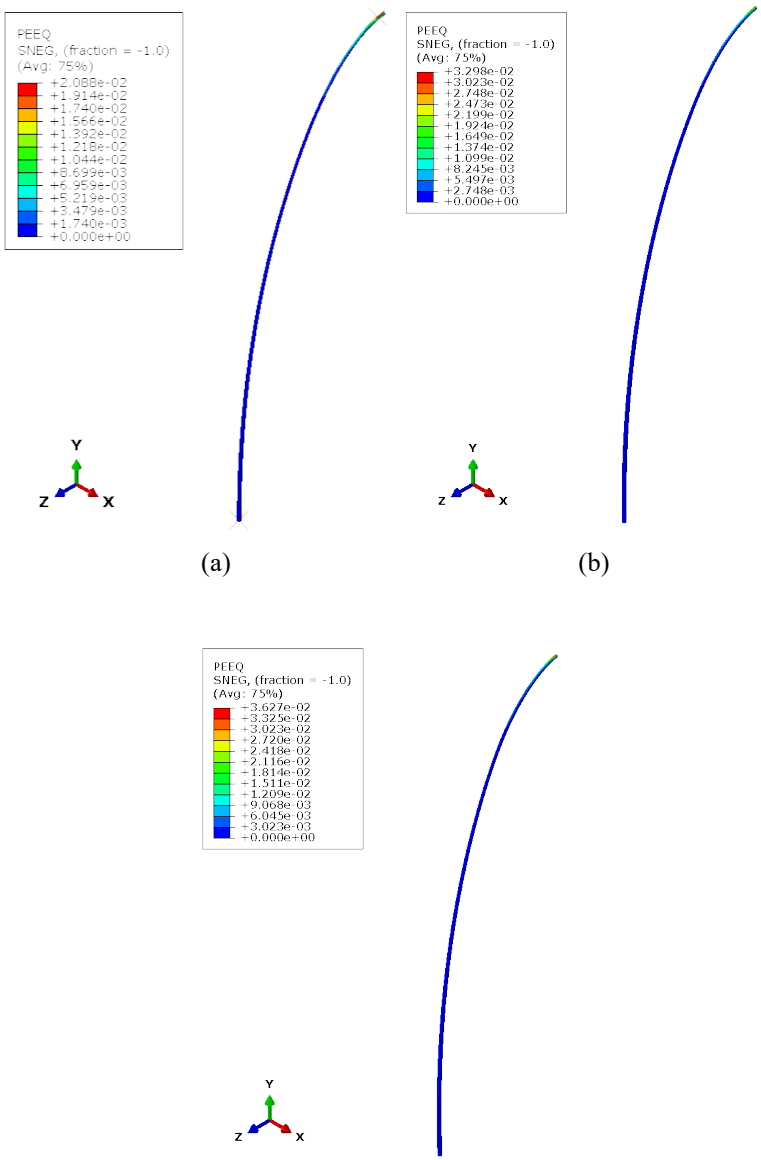

Figure 11. Strain contours of tapered cylindrical shells with different lengths: (a) 10 m, (b) 30 m, and (c) 50 m.

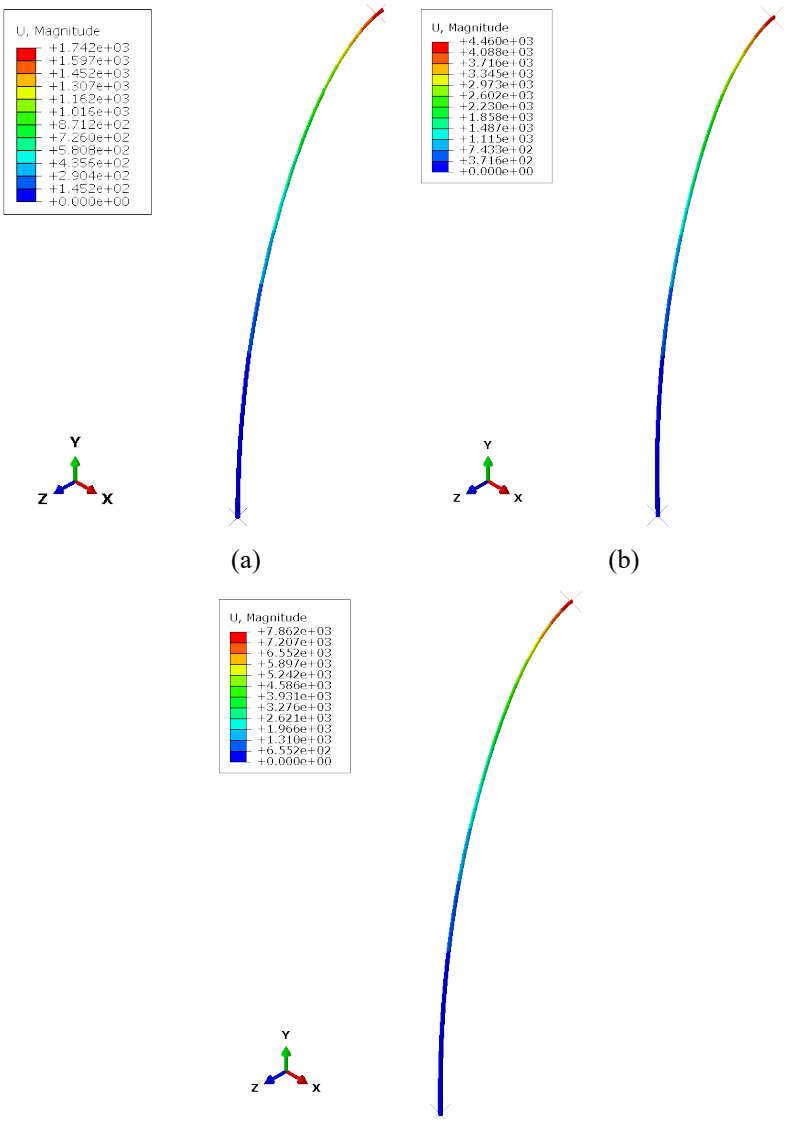

Figure 12. Displacement contours of tapered cylindrical shells with different lengths: (a) 10 m, (b) 30 m, and (c) 50 m.

4.3. L/D₀ Variations

The results of this variation were compared using a bending moment versus curvature graph, as seen in Figure 13. The selected model incorporates varying L/D_0 ratios while keeping the other geometric parameters and material yield stresses identical. The graph shows that the ultimate moment increases as the pipe's bottom diameter increases (or the L/D_0 ratio decreases). The highest bending moments achieved for pipes with L/D_0 ratios of 200, 300, and 400 are 4.097 kN·m, 9.750 kN·m, and 34.58 kN·m, respectively. The increase is more noticeable between the pipes with L/D_0 ratios of 200 and 300 than between those with L/D_0 ratios of 300 and 400. This is because the effect of increasing the ratio becomes less noticeable as the value grows more prominent. The diameter or L/D_0 ratio also affects the geometry's thickness ratio, making slenderer geometries more prone to collapse from buckling, accompanied by yielding. This finding is consistent with the discovery made by Li and Kim (2022).

Figure 14 displays the stress contours of pipes with varying L/D_0 ratios during the elastic phase, plastic deformation phase, and critical phase. It can be observed that the stress contour with a slenderer geometry had a wider distribution of stresses on the structure. As the slenderness increases, the effective cross-sectional area resisting bending decreases relative to the length, making it easier for the pipe to reach its yield point under lower moments. The reduced cross-section also means that even small loads can induce noticeable deflections, which makes it more elastic.

In Figure 15, the slenderer the pipe, the higher its maximum strain in its structure. A higher slenderness ratio (larger L/D_0 ratio) increases the likelihood of buckling earlier under load, as seen in Figure 13, and can lead to higher strains. The strain distribution on the slenderer pipe is also non-uniform due to varying moments of inertia along its length. This non-uniformity can lead to higher strains at the end of high curvature.

Figure 16 shows the displacement contours for various L/D_0 ratios. The figure shows that the slender pipe or one with a higher L/D_0 ratio exhibits more significant displacement under the same bending load than the pipe with a larger diameter. This is due to the reduced moment of inertia associated with slender designs, which makes them more flexible and prone to more considerable deflections. This aligns with the strain contours, indicating a direct proportionality between strain and displacement.

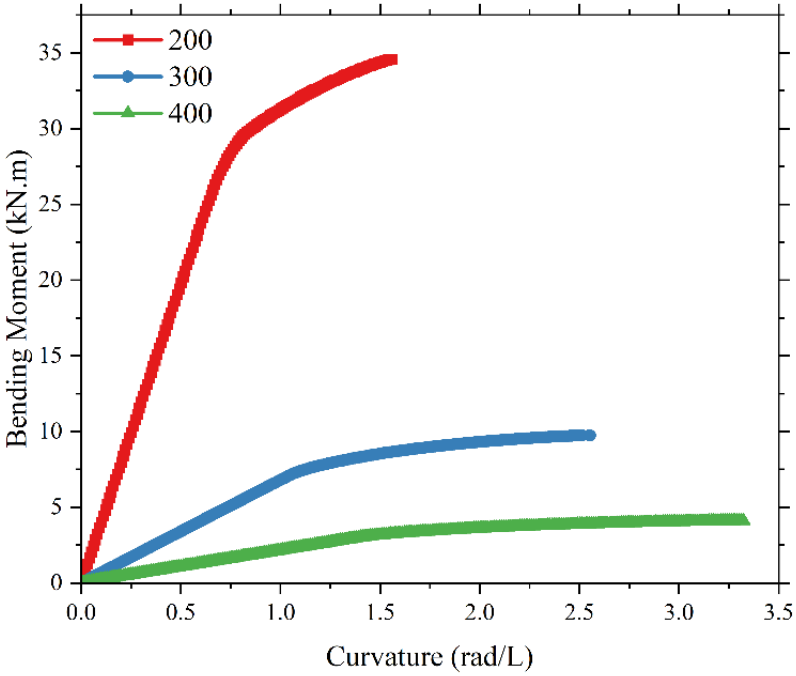

Figure 13. Moment-curvature graph for the length-to-bottom diameter ratio (L/D_0) variation.

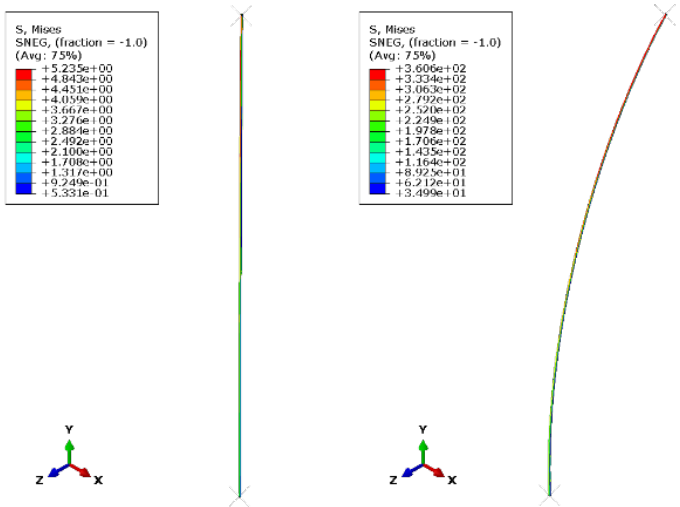

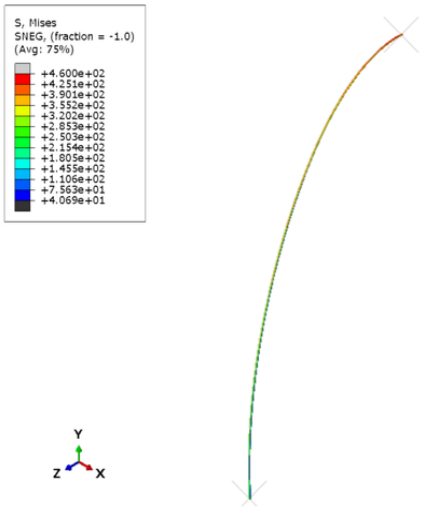
S, Mises
SNEG, (fraction = -1.0)
(Avg: 75%)
+4.600e+02
+4.251e+02
+3.901e+02
+3.552e+02
+3.202e+02
+2.853e+02
+2.503e+02
+2.154e+02
+1.805e+02
+1.455e+02
+1.106e+02
+7.563e+01
+4.069e+01
Y
Z
X

(a)

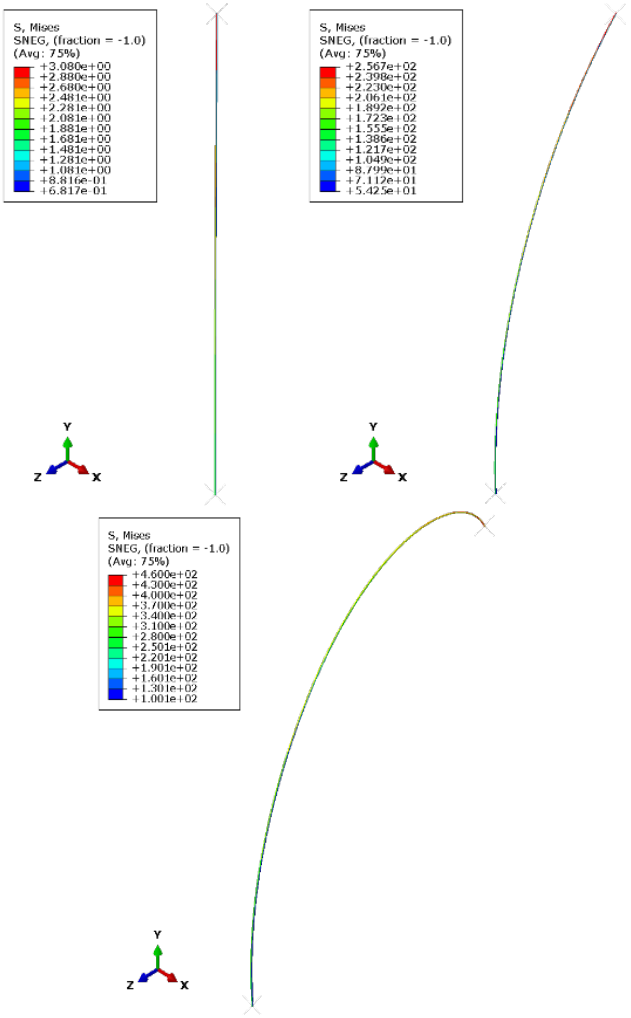
S, Mises
SNEG, (fraction = -1.0)
(Avg: 75%)
+3.080e+00
+2.880e+00
+2.680e+00
+2.481e+00
+2.281e+00
+2.081e+00
+1.881e+00
+1.681e+00
+1.481e+00
+1.281e+00
+1.081e+00
+8.816e-01
+6.817e-01
Y
Z
X
S, Mises
SNEG, (fraction = -1.0)
(Avg: 75%)
+2.567e+02
+2.398e+02
+2.230e+02
+2.061e+02
+1.892e+02
+1.723e+02
+1.555e+02
+1.386e+02
+1.217e+02
+1.049e+02
+8.799e+01
+7.112e+01
+5.425e+01
Y
Z
X
S, Mises
SNEG, (fraction = -1.0)
(Avg: 75%)
+4.600e+02
+4.300e+02
+4.000e+02
+3.700e+02
+3.400e+02
+3.100e+02
+2.800e+02
+2.501e+02
+2.201e+02
+1.901e+02
+1.601e+02
+1.301e+02
+1.001e+02
Y
Z
X

(b)

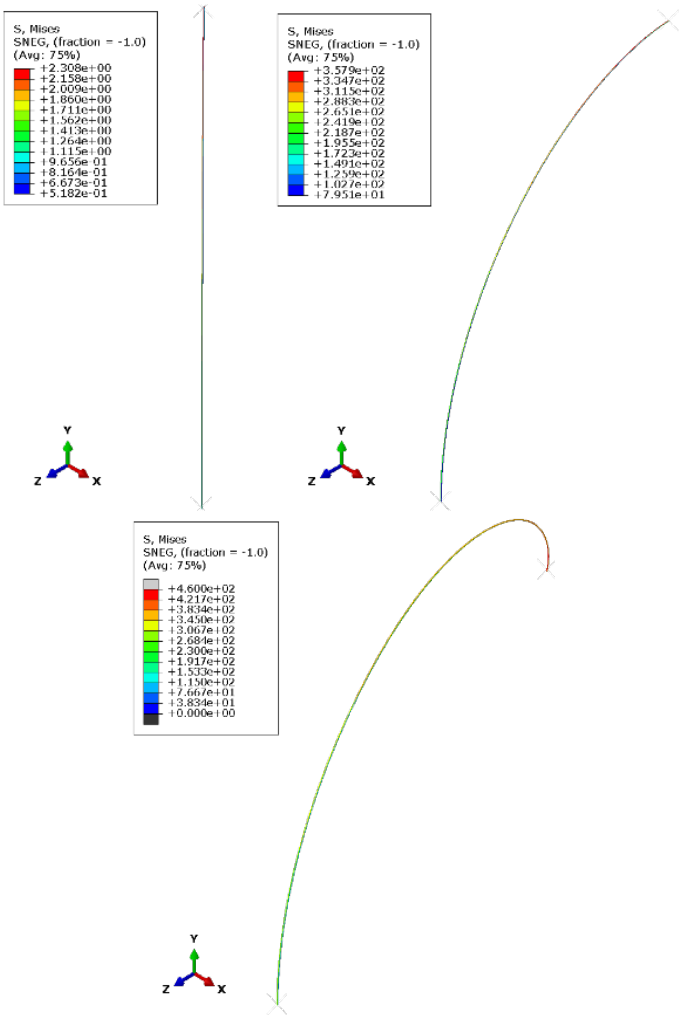

(c)

Figure 14. Stress contours of tapered cylindrical shells with different L/D_0 ratios: (a) 200, (b) 300, and (c) 400.

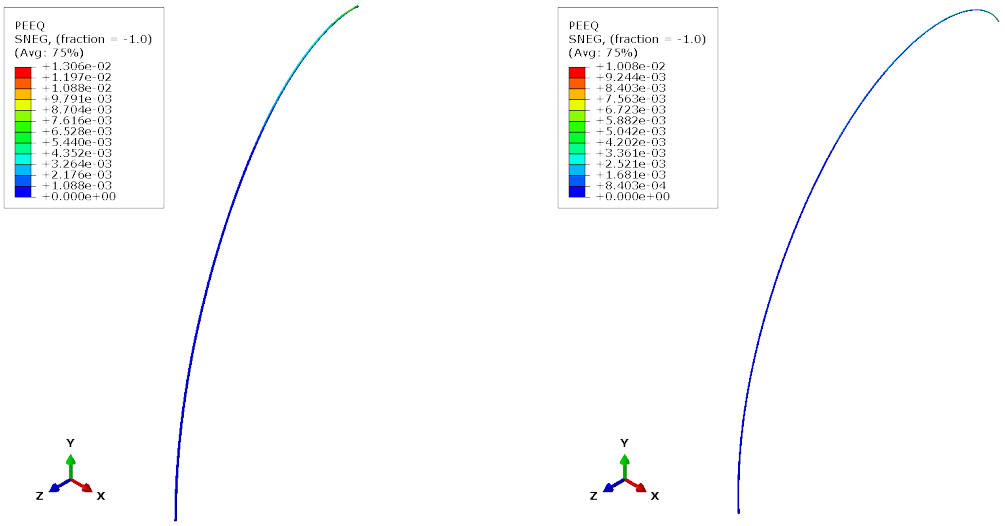

(a) (b)

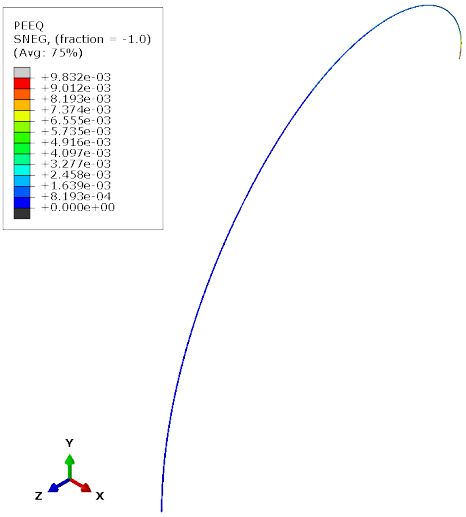

(c)

Figure 15. Strain contours of tapered cylindrical shells with different L/D_0 ratios: (a) 200, (b) 300, and (c) 400.

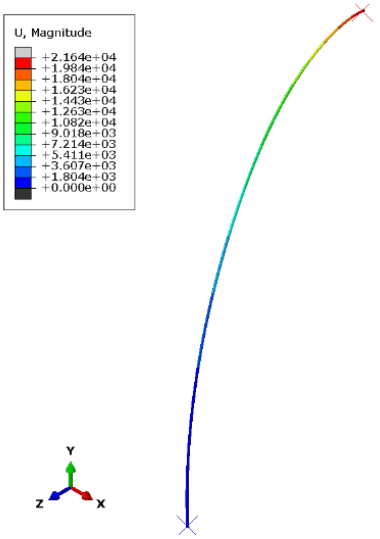

(a)

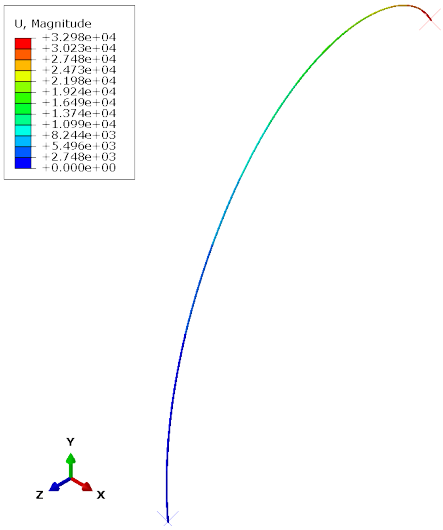

(b)

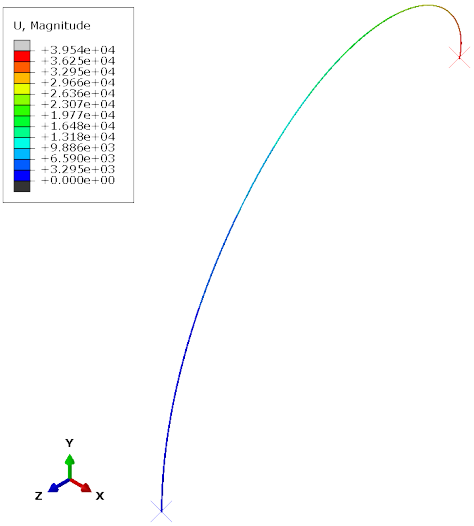

(c)

Figure 16. Displacement contours of tapered cylindrical shells with different L/D_0 ratios: (a) 200, (b) 300, and (c) 400.

4.4. D_1/D_0 Variations

The results of this variation were compared using a bending moment versus curvature graph, as seen in Figure 17. The selected model incorporates varying D_1/D_0 ratios while keeping the other geometric parameters and material yield stresses identical. The graph shows that the ultimate moment also increases with the increase in the diameter of the tapered pipe's upper section. This effect occurred due to varying stress concentrations along its length, resulting from changes in diameter. The larger diameter sections typically experienced higher stresses than the smaller diameter sections under the same bending load.

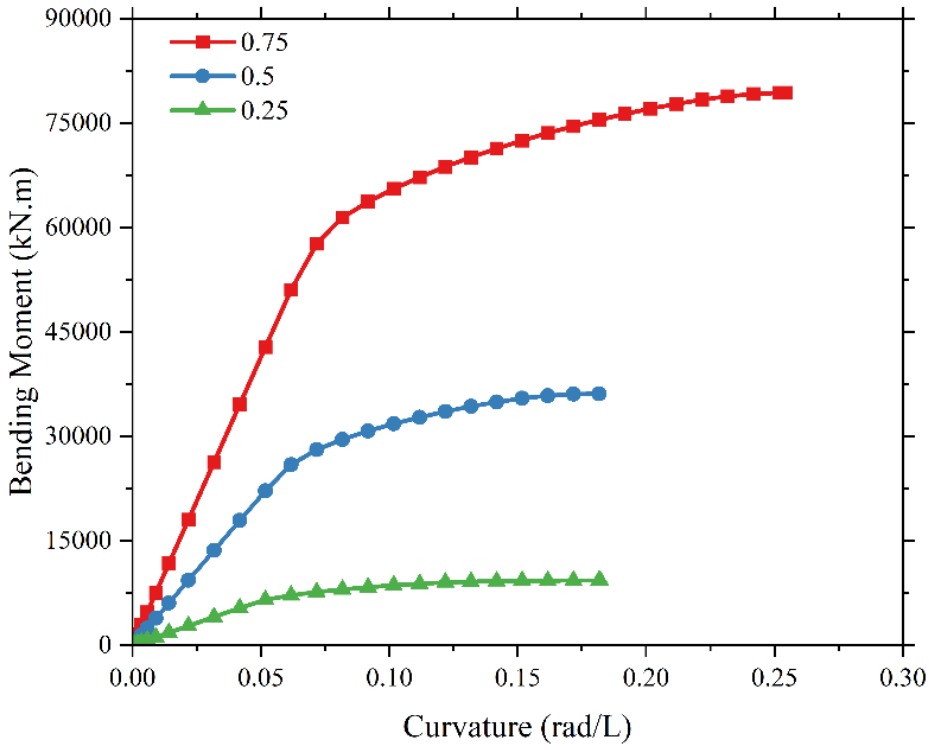

Figure 17. Moment-curvature graph for the variation in the upper diameter to bottom diameter ratio (D_1/D_0).

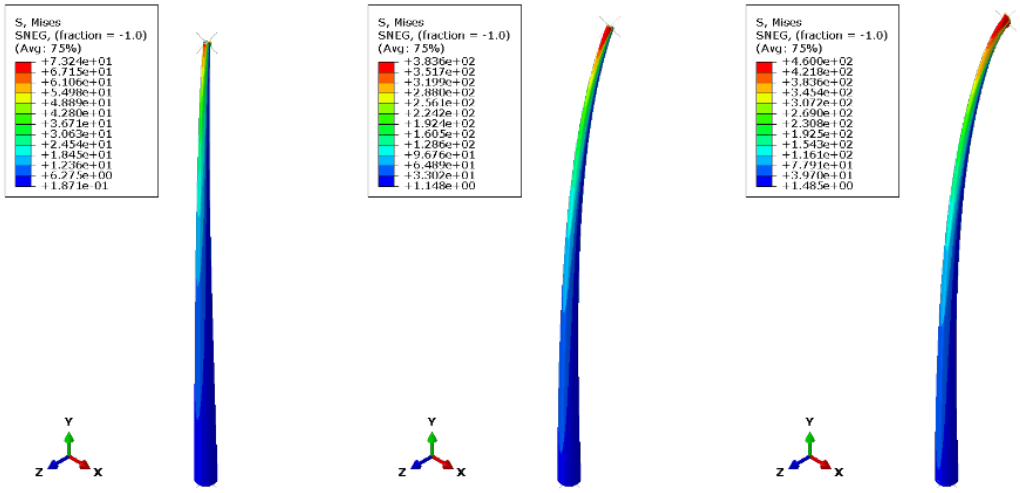

cale factor = 10 (a)

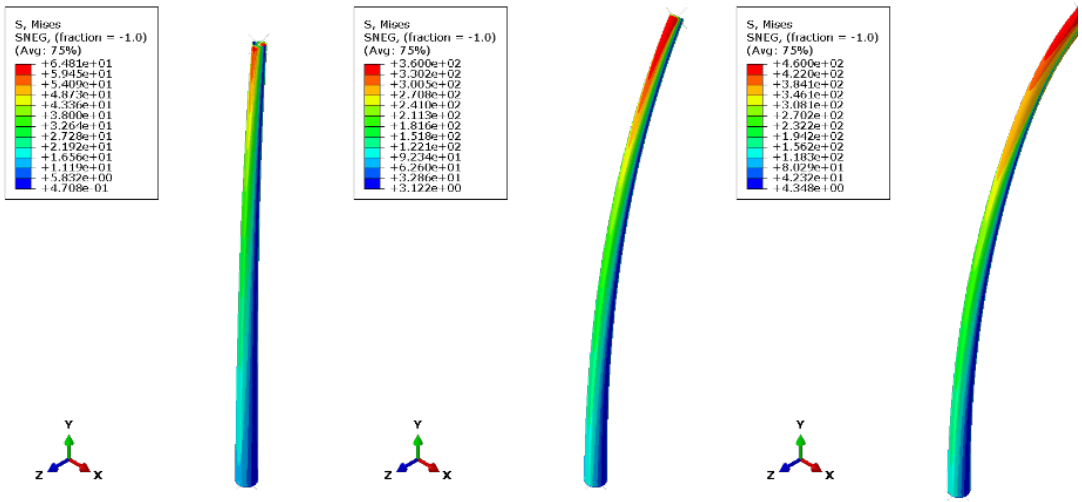

Scale factor = 10 (b)

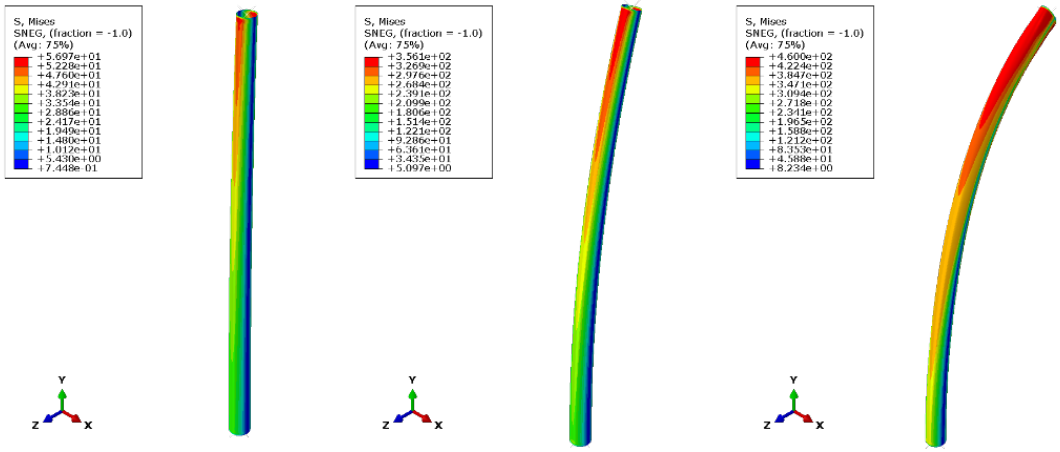

Scale Factor = 5 (c)

Figure 18. Stress contours of tapered cylindrical shells with different D_1/D_0 ratios: (a) 0.25, (b) 0.5, and (c) 0.75.

Figure 18 shows the stress contour of pipes with varying D_1/D_0 ratios during the elastic phase, plastic

deformation phase, and critical phase. The critical moments for pipes with D_1/D_0 ratios of 0.25, 0.5, and 0.75 are 9324.4 kN·m, 36119 kN·m, and 79366 kN·m, respectively, with increases from the plastic deformation phase to the critical moment of 42%, 62%, and 85%. It can be observed that the increase becomes more pronounced as the taper becomes more gradual. This is because a more gradual taper makes the pipe more susceptible to buckling under load, which increases its resistance during the plastic deformation phase before reaching the critical peak. Figure 18 also illustrates a shift in the stress distribution along the pipe's length. As the taper increases, the position of the cross-section under bending shifts. Pipes with a steeper taper experience higher localized stresses at the transition points than those with a more gradual taper. From the contours, it can be seen that in $D_1/D_0 = 0.25$, the red stress bands are highly concentrated near the transition zone, while in D_1/D_0 is 0.5 and 0.75 the stresses spread more gradually along the height, indicating a redistribution of load. The gradual taper results in a broader stress field with smoother gradients, whereas the steep taper shows sharp stress localization, marking potential failure zones

Figure 19 shows the strain contours of a tapered pipe with varying D_1/D_0 ratios. It can be observed that the tapered pipe with a lower D_1/D_0 ratio (or steeper taper) exhibits higher peak strain. This occurs because a steeper taper creates more significant stress concentrations at the transition points where the diameter changes rapidly. A more gradual taper distributes stress evenly along the pipe's length, resulting in a lower peak strain. The contour plots illustrate that the steep taper (D_1/D_0 = 0.25) leads to the formation of intense, localized strain zones characterised by sudden colour transitions in the vicinity of the diameter transition. Conversely, the gradual taper ($D_1/D_0 = 0.75$) results in more uniform and subtle alterations in strain colouration along the shell. This finding indicates that the steep taper undergoes more localised deformation, whereas the gradual taper spreads the strain over a larger region.

Figure 20 shows the displacement contours of a tapered pipe with varying D_1/D_0 ratios. It can be observed that the steeper-tapered pipe experiences less displacement under bending loads compared to a more gradual-tapered pipe. In a steeper-tapered pipe, the cross-sectional area decreases more rapidly, which can reduce the overall resistance to bending. This reduction in stiffness contributes to increased deflection under loading conditions. This results in lower displacements under similar loading conditions compared to a more gradual taper.

As demonstrated by the displacement contours, the pipe with D_1/D_0 is 0.25 exhibits limited deflection, localised in proximity to the base, with displacement colours concentrated in a diminutive zone. Conversely, the pipe with D_1/D_0 is 0.75 demonstrates broader zones of high displacement extending further up the shell, indicating global deformation. This visual difference underscores the pivotal role of taper ratio in dictating whether the response is predominantly characterised by localised or distributed displacement.

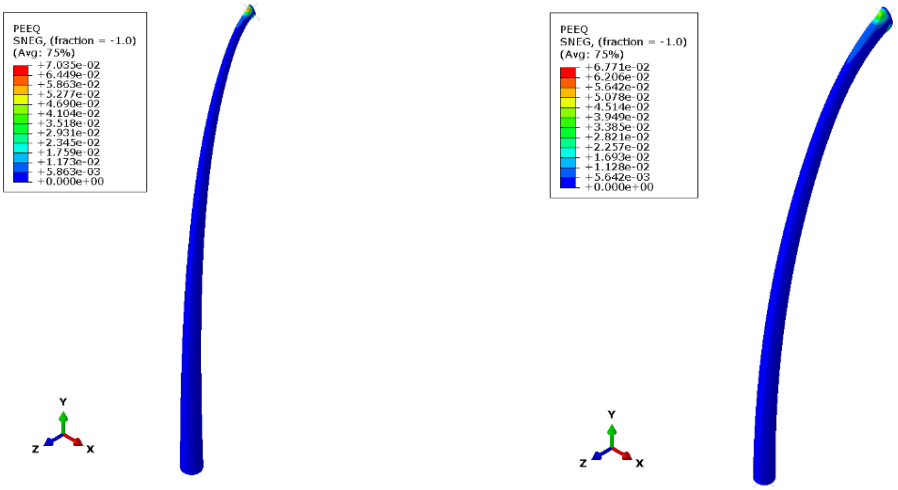

(a) (b)

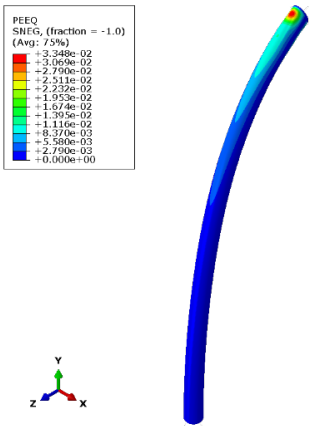

(c)

Figure 19. Strain contours of tapered cylindrical shells with different D_1/D_0 ratios: (a) 0.25, (b) 0.5, and (c) 0.75.

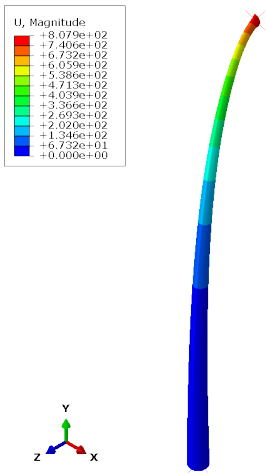

(a)

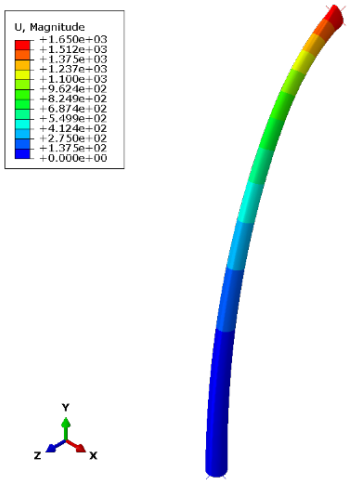

(b)

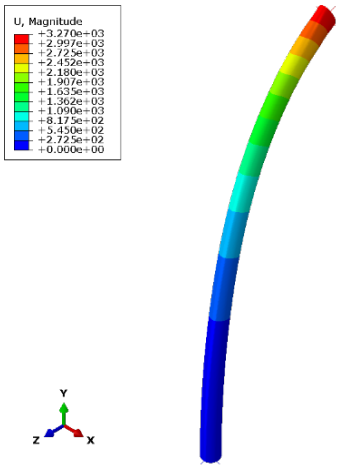

(c)

Figure 20. Displacement contours of tapered cylindrical shells with different D_1/D_0 ratios: (a) 0.25, (b) 0.5, and (c) 0.75.

4.5. D_0/t Variations

The results of this variation were compared using a bending moment versus curvature graph, as seen in Figure 21. The selected model incorporates varying thicknesses while keeping the other geometric parameters and material yield stresses identical. The graph demonstrated that the ultimate bending moment rose significantly with an increase in thickness (or a decrease in the D_0/t ratio). This is because a thicker geometry possesses a much higher moment of inertia, allowing it to endure considerably greater bending stresses up to its yield point. It was also evident that the plastic deformation region in thicker geometries was significantly more prominent than in thinner ones. Increasing a structure's thickness expands the area that can undergo plastic deformation, allowing for a more extensive deformation zone. Figure 21 also shows the bending moments during the critical phase for pipes with D_0/t ratios of 50, 100, 150, and 200, which are 7812.6 kN·m, 3805.6 kN·m, 2455.4 kN·m, and 1797.7 kN·m, respectively. The increases from the plastic deformation phase to the critical moment are 18%, 15%, 12%, and 20%, respectively.

Figure 22 shows the stress contours of pipes with different D_0/t ratios during the elastic, plastic deformation, and critical phases. A shift in stress distribution is observed, with the maximum stress at the top moving toward the ends and at the bottom shifting toward the center due to bending, where one side is in tension and the other in compression. The contours indicate that thicker pipes (lower D_0/t) develop broader stress regions with smoother gradients. In comparison, thinner pipes (higher D_0/t) display narrow, high-intensity stress bands concentrated near the base and wall edges, indicating a greater tendency toward local buckling.

The corresponding strain contours in Figure 23 show that thinner shells exhibit sharper and more localized strain, particularly near the top region where stresses are highest. In contrast, thicker shells display more diffuse and evenly distributed strain across the section. This confirms that strain localization intensifies as wall thickness decreases, making thinner shells more prone to early deformation. Figure 24 presents the displacement contours. Thin shells (higher D_0/t) experience larger global deflections extending along the shell height, while thicker shells deform in a more localized manner near the loaded region. This behavior is explained by the higher moment of inertia of thicker pipes, which increases stiffness and reduces overall deflection under bending.

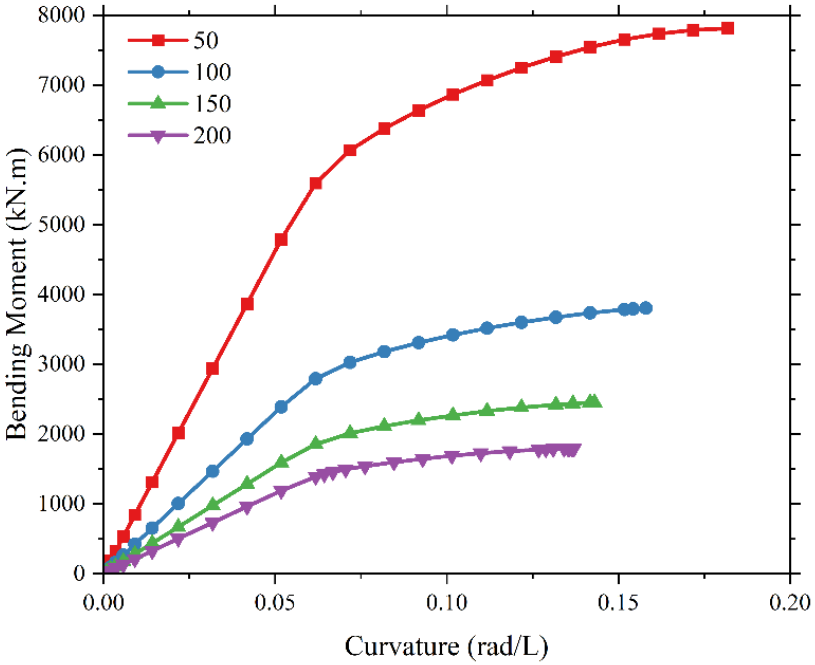

Figure 21. Moment-curvature graph for the variation of bottom diameter to thickness ratio (D_0/t).

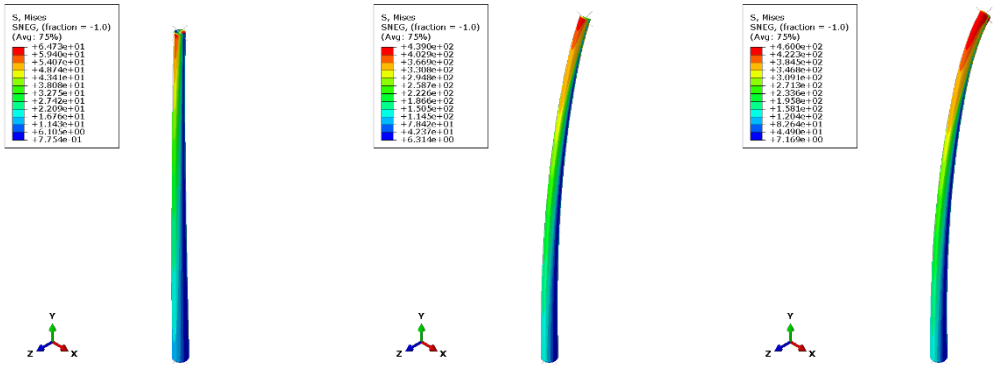

Scale factor = 5 (a)

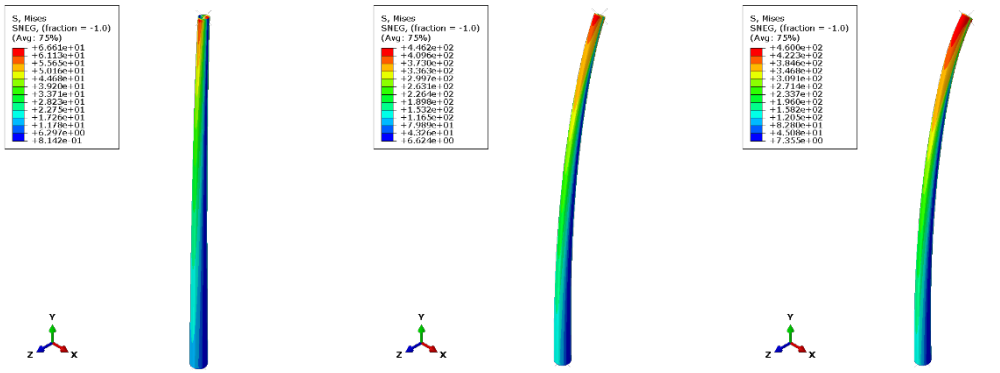

Scale factor = 5 (b)

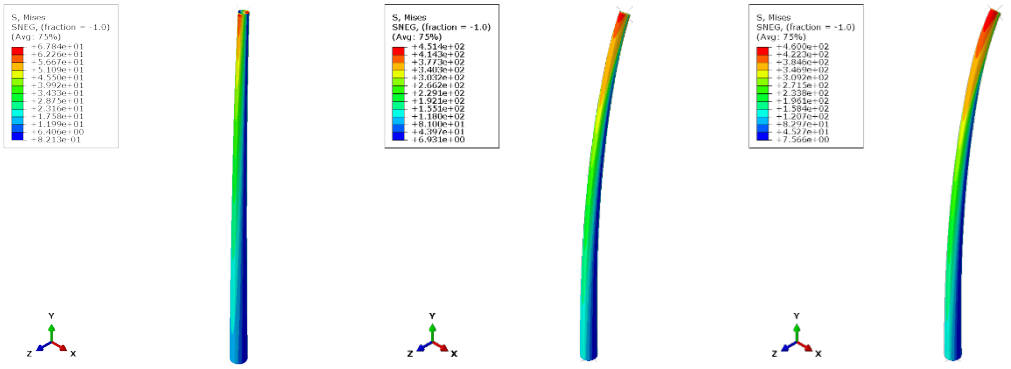

Scale factor = 5 (c)

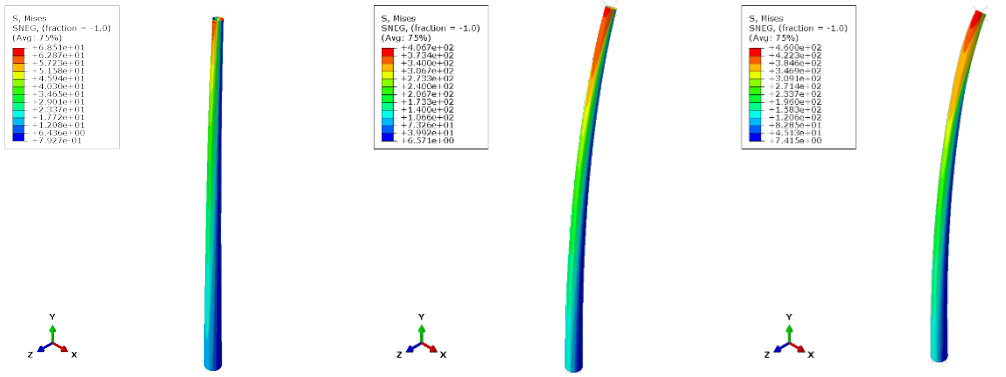

Scale factor = 5 (d)

Figure 22. Stress contours of tapered cylindrical shells with different D_0/t ratios: (a) 50, (b) 100, (c) 150, and (d) 200.

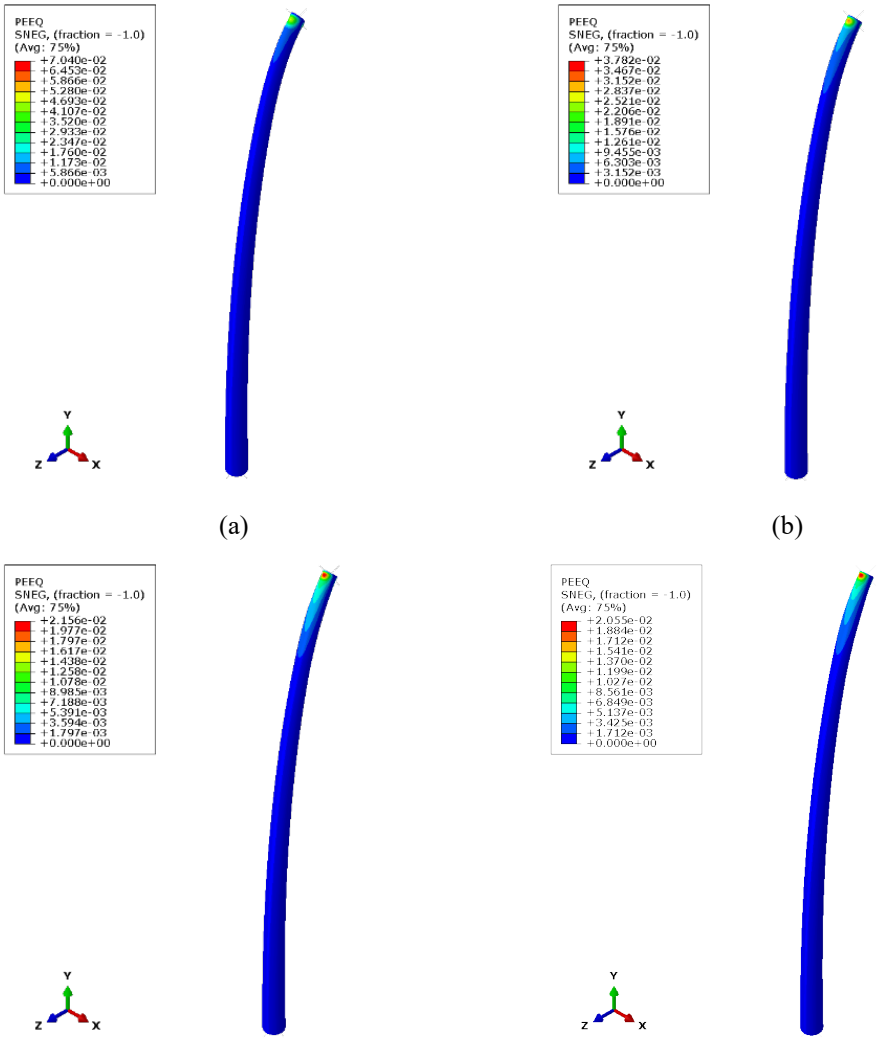

Figure 23. Strain contours of tapered cylindrical shells with different D_0/t ratios: (a) 50, (b) 100, (c) 150, and (d) 200.

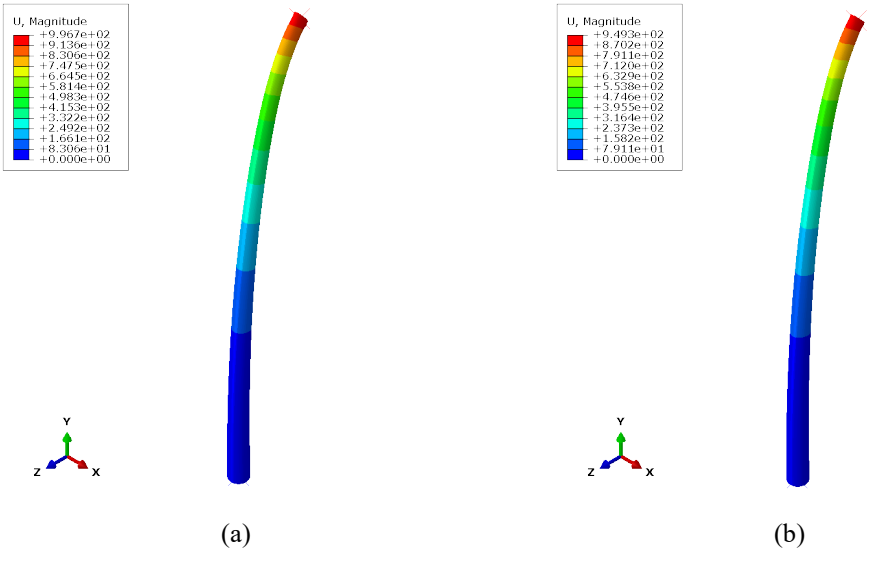

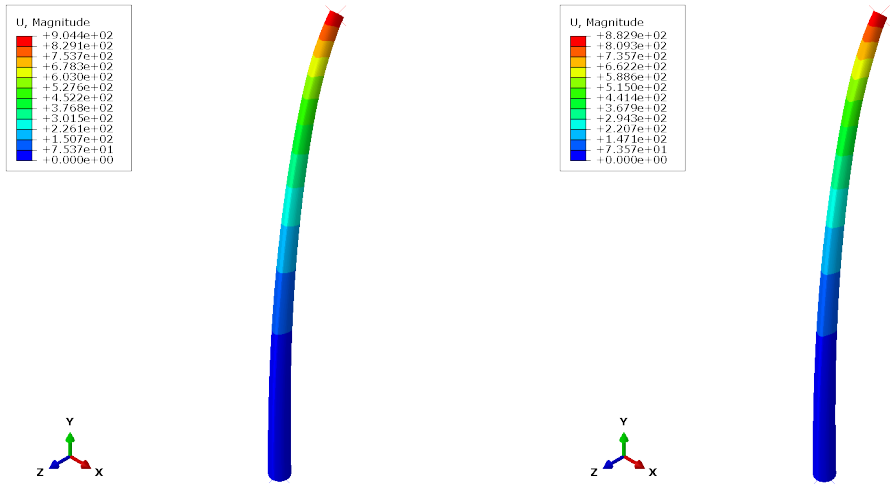

(c) (d)

Figure 24. Displacement contours of tapered cylindrical shells with different D_0/t ratios: (a) 50, (b) 100, (c) 150, and (d) 200.

4.6. Yield Stress Variations

The results of this variation were compared using a bending moment versus curvature graph, as seen in Figure 25. The selected model incorporates varying yield stress while maintaining identical geometric parameters. It can be observed that higher yield stresses correspond to higher ultimate bending moments. Higher yield stresses enable the tapered pipes to withstand greater bending moments before yielding or failing. Figure 25 also shows that the pipes exhibit similar bending strength until the plastic deformation phase, as they share the same material properties except for their yield stress. The highest critical moment is observed in the pipe with a yield stress of 355 MPa, reaching 278.7 kN·m, while the lowest is in the pipe with a yield stress of 235 MPa, with a moment of 196.1 kN·m. The average increase in the moment from the plastic deformation phase to the critical phase is 24%.

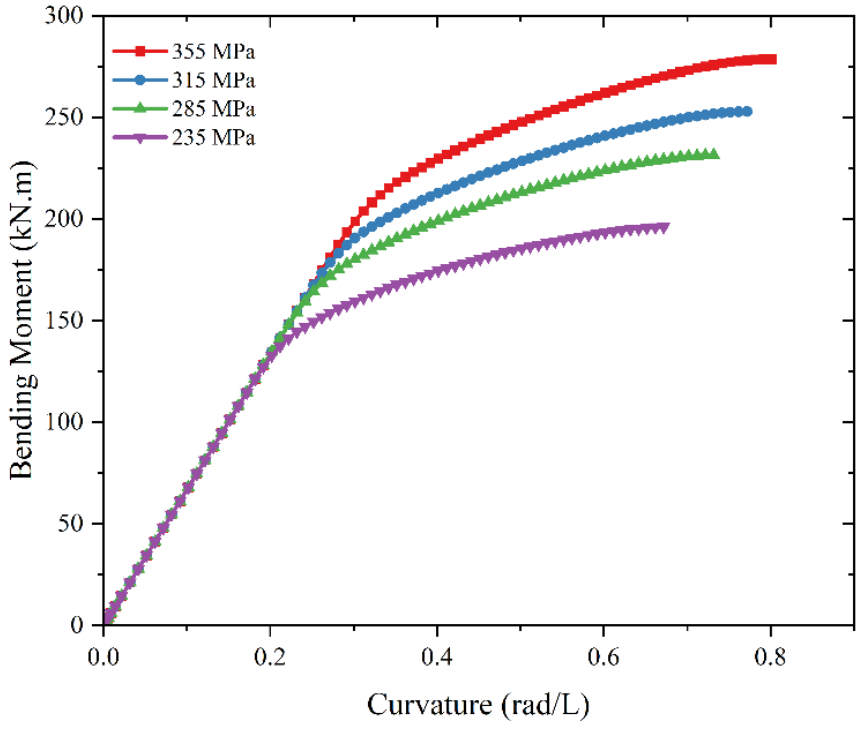

Figure 25. Moment-curvature graph for the material yield stresses ($\boldsymbol{\sigma_y}$) variation.

Figure 26 shows the stress contours of pipes with varying yield stresses (355, 315, 285, and 235 MPa) across the elastic, plastic, and critical phases. Pipes with higher yield stress sustain broader elastic regions before yielding, as indicated by wider areas of uniform stress distribution. In contrast, lower yield stress pipes exhibit localized high-stress zones near the fixed base at earlier stages. This finding lends further credence to the hypothesis that higher yield strength enables the shell to withstand greater bending loads prior to plastic deformation.

The corresponding strain contours in Figure 27 demonstrate that, despite the overall distribution patterns remaining similar due to identical geometry, the peak strain values differ. The pipe with a yield stress of 355 MPa develops more widespread strain zones along its height, while the pipe with a yield stress of 235 MPa shows sharper and more localized strain near its base. This emphasizes that stronger materials can accommodate greater deformation before local buckling occurs. Figure 28 provides further illustration of the displacement contours, whereby higher yield stress pipes demonstrate larger global deflections extending along the shell, whilst lower yield stress pipes undergo localized displacement concentrated at the base. Collectively, these observations indicate that increasing yield stress not only raises the ultimate bending capacity but also alters the deformation behaviour, allowing more distributed stress, strain, and displacement patterns before critical failure.

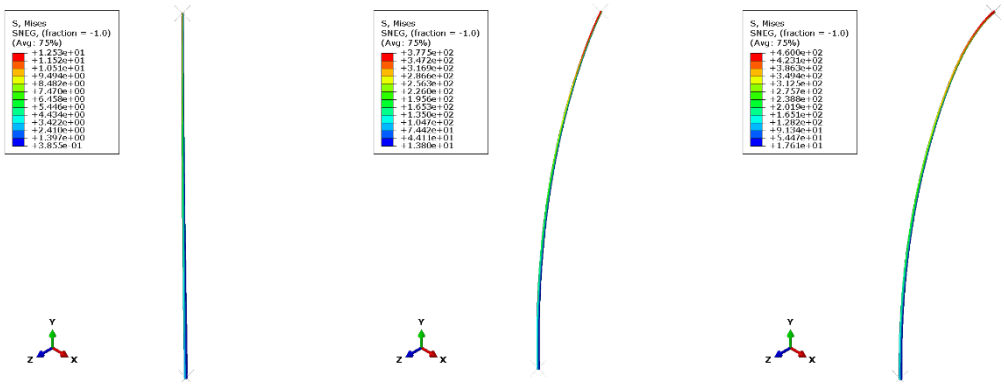

Scale factor = 2 (a)

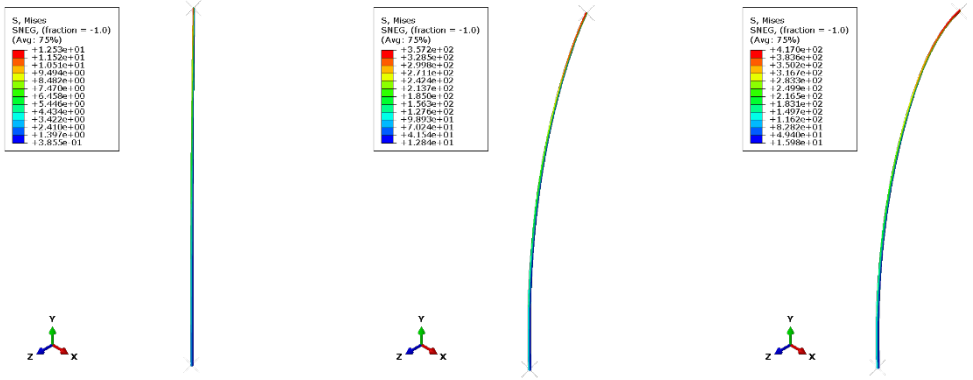

Scale factor = 2 (b)

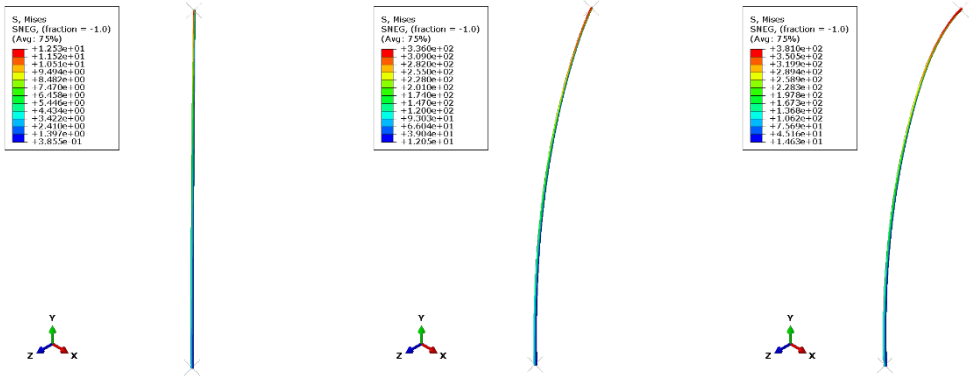

Scale factor = 2 (c)

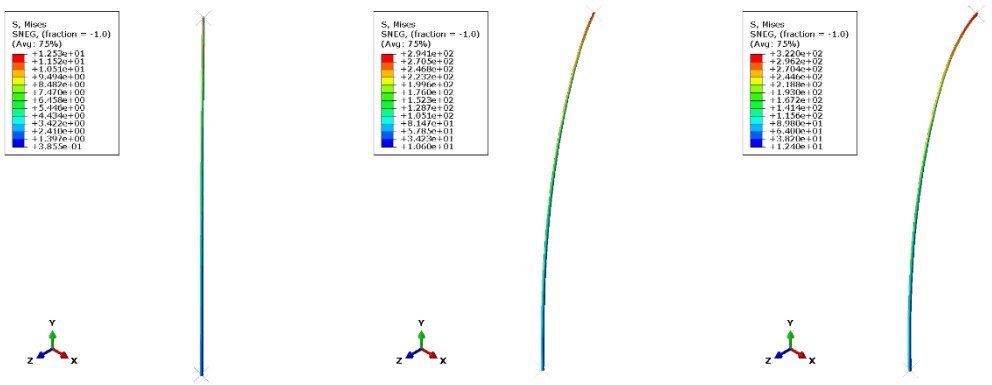

Figure 26. Stress contours of tapered cylindrical shells with different yield stresses: (b) 355 MPa, (b) 315 MPa, (c) 285 MPa, and (d) 235 MPa.

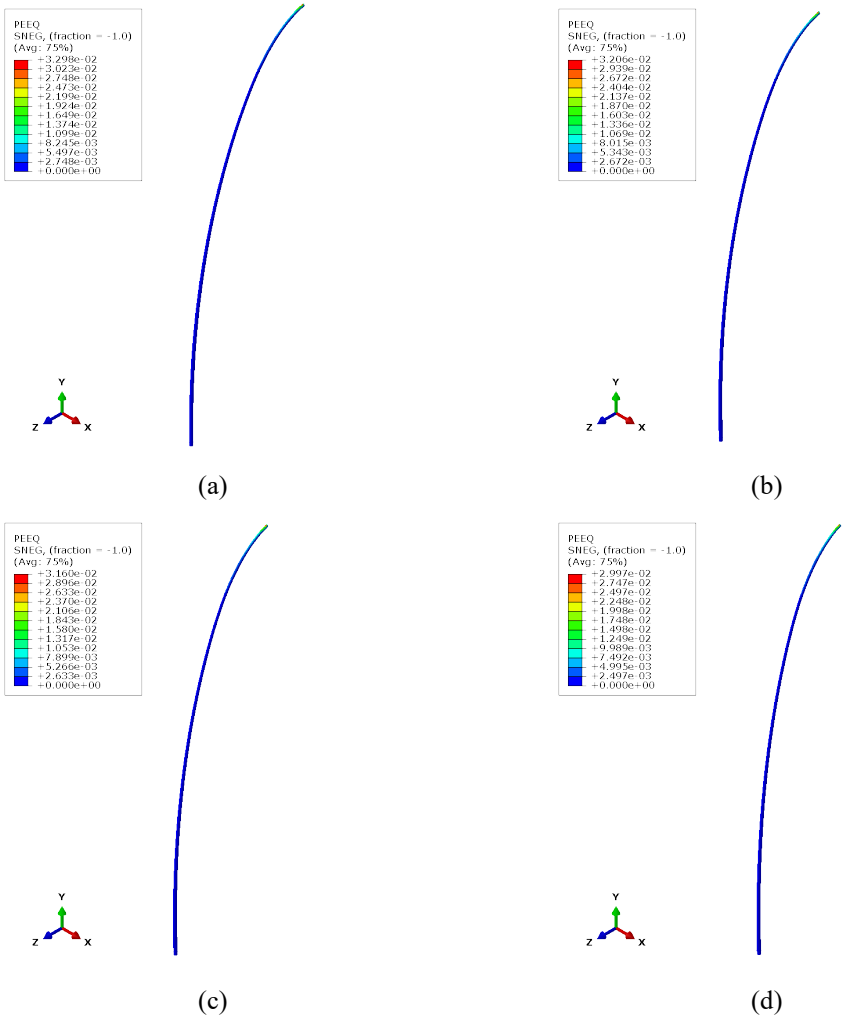

Figure 27. Strain contours of tapered cylindrical shells with different yield stresses: (b) 355 MPa, (b) 315 MPa, (c) 285 MPa, and (d) 235 MPa.

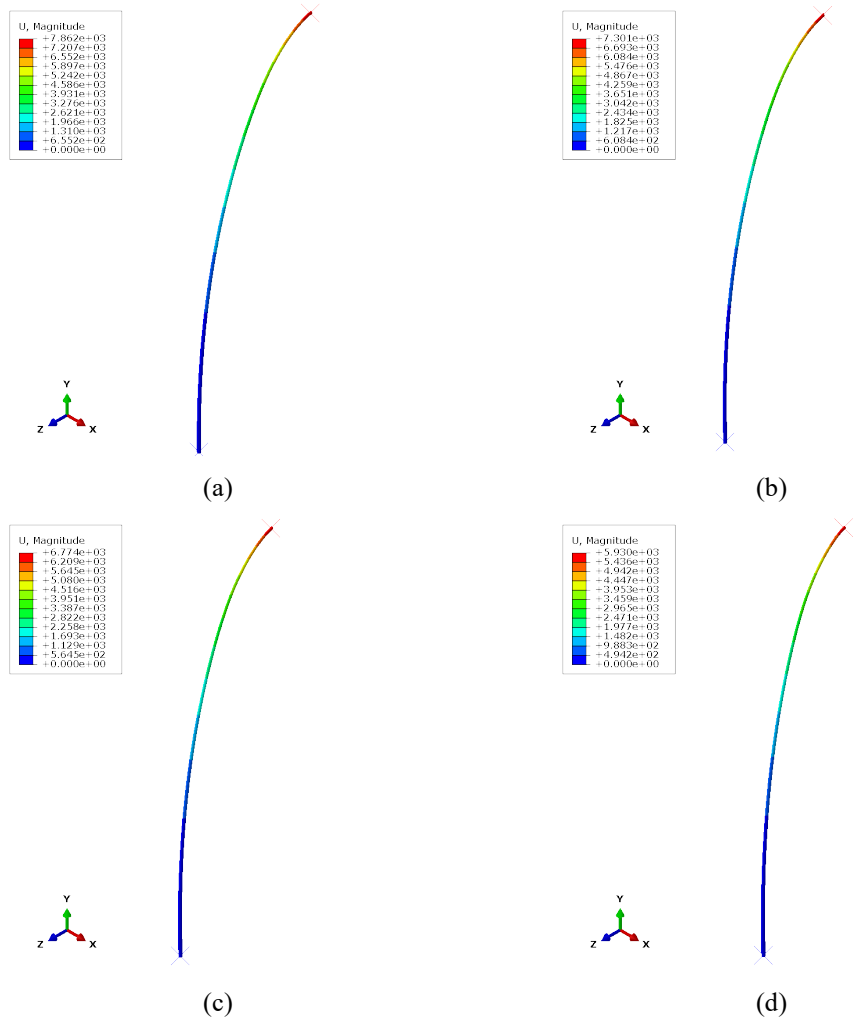

Figure 28. Displacement contours of tapered cylindrical shells with different yield stresses: (b) 355 MPa, (b) 315 MPa, (c) 285 MPa, and (d) 235 MPa.

4.7. Adaptation of Classical Formulations for Tapered Shells

The majority of classical analytical formulations that describe the bending and buckling of cylindrical shells were initially developed for prismatic geometries with uniform cross-sections and constant wall thickness. Such formulations include Brazier's moment for ovalization-induced stiffness reduction, Timoshenko's elastic buckling for thin-walled cylinders, and the Reference Resistance Design (RRD) framework for plastic collapse. These theories inherently neglect the geometric non-uniformity and stiffness variation along the shell axis that characterise tapered configurations.

In the present study, these classical frameworks were not directly implemented; instead, they were conceptually adapted to account for the influence of tapering through key non-dimensional parameters (L/D_0, D_1/D_0, and D_0/t). The fundamental physical interpretations of bending stiffness and local shell slenderness from the classical models were retained. At the same time, geometric non-uniformity was introduced by allowing the radius and wall thickness to vary along the shell length. This enables the FEM-based parametric analysis to inherently capture the nonlinear stiffness distribution and stress gradients induced by tapering, thus extending the applicability of classical shell theory to non-prismatic configurations.

Large-scale finite element method (FEM) simulations thus serve as a numerical extension of these classical theories, evaluating the evolution of established bending–buckling relationships under geometric non-uniformity. The resulting moment-curvature behaviour obtained from the finite element method (FEM) provides the quantitative foundation for the regression analysis presented in Section 4.2. This analysis generalises the classical formulations by embedding the taper ratio and shell slenderness into a unified predictive expression. Consequently, while the Brazier-Timoshenko-RRD formulations remain valuable for conceptual understanding and validation, they are here extended and reinterpreted

within a non-prismatic framework. The proposed regression model can thus be regarded as a generalized formulation of bending resistance that accounts for taper-induced stiffness gradients, thereby effectively bridging the gap between idealised analytical solutions and realistic tapered wind turbine tower geometries.

The transition between elastic and plastic responses in tapered shells follows a progressive deformation sequence, further supporting this theoretical adaptation. When subjected to bending loads, the structure initially exhibits elastic buckling behaviour, as predicted by Timoshenko's theory, with a stiffness distribution that conforms to this theory. As the curvature increases, local yielding commences in regions of larger diameter, consistent with the stiffness reduction associated with Brazier's ovalization mechanism. At this stage, the results of the non-linear finite element method (FEM) capture stress redistribution and the formation of plastic hinges until global collapse. This is consistent with the plastic resistance concept described by the RRD framework. This sequential evolution from elastic to plastic regimes validates the physical consistency of the selected non-dimensional parameters (L/D_0, D_1/D_0, D_0/t, and σ_γ) and supports their role in representing both geometric stiffness variation and material yielding effects.

The isotropic elastic-plastic model employed in this study provides a controlled framework for isolating and quantifying these fundamental behaviors. Although weld-induced imperfections and residual stresses, which are typical of practical steel towers, were not explicitly modelled, this simplification enables the focus to remain on the geometric and material nonlinearities governing global bending capacity. The incorporation of such fabrication-related effects would necessitate additional assumptions and manufacturing-specific data, which are reserved for future work. Nevertheless, the present findings establish a robust theoretical and numerical foundation upon which subsequent investigations may assess imperfection sensitivity and practical design margins for real wind turbine tower structures.

4.8. Regression Analysis

The nonlinear kinematic, theoretical strength physically guides the regression formulation developed in this section, and plastic collapse relations discussed in Section 2. These formulations establish the functional dependence of bending capacity on geometric ratios and yield stress, which are incorporated in the regression equations (Eqs. 43 - 45) as governing non-dimensional parameters (L/D_0, D_1/D_0, D_0/t, and σ_γ). Conversely, the Reference Resistance Design (RRD) and transversely anisotropic elasticity formulations are not directly applied, but they serve as a supporting theoretical background for a comparative understanding. The correlation between these governing equations and the proposed empirical model is summarized in Table 5. While the classical analytical equations (Eqs. 35 - 40) provide a theoretical framework for prismatic shells, they are limited in their ability to represent geometric non-uniformity and taper-induced stiffness variation. It is evident that the regression-based formulation developed herein functions to generalize the classical theories into a unified empirical model. This model is capable of predicting the ultimate bending capacity of tapered cylindrical shells.

To ensure comparability among models with varying geometric and material properties, the reaction moment obtained from FEM simulations was normalized by $M_n = D^2 t \sigma_y$. This normalization provides a dimensionally consistent and physically meaningful scaling that isolates the geometric and material influences on bending capacity. It also aligns with established shell bending conventions, allowing direct comparison between the present tapered configurations and classical prismatic cases. While additional deformation indicators, such as ovalization and displacement profiles, were monitored for qualitative validation, they were not included in the normalization, as their effects are inherently reflected in the moment–curvature relationship. Therefore, normalization by $D^2 t \sigma_y$ is deemed sufficient for FEM validation and ensures consistent interpretation of regression results across all configurations.

Table 5. Correlation Between Governing Equations and the Developed Regression Model.

Source	Theoretical Concept	Role in Regression Model
Eq. (1-6)	Nonlinear kinematics describing curvature–strain–moment relations and deformation compatibility in cylindrical shells.	Serves as the theoretical foundation for defining the bending moment parameter in the regression equations (Eqs. 43-45), linking curvature (κ), stiffness (EI), and slenderness (L/D_0) to the ultimate bending response.

Eq. (7-9)	Theoretical strength estimation for cylindrical shells under bending and axial stress.	Provides the geometric dependency formulation implemented in Eq. (44), establishing how diameter-to-thickness ratio (D_0/t), taper ratio (D_1/D_0), and yield stress (σ_Y) influence the ultimate moment capacity.
Eq. (10-11)	Plastic collapse theory defines the transition from elastic to fully plastic bending and the ultimate moment (M_p).	Defines the ultimate capacity criterion used as the dependent variable in Eqs. (43 - 44), representing the limit-state bending strength of the shell.
Eq. (12-15)	Normalized moment capacity formulation to eliminate geometric scaling bias.	Provides the normalization scheme adopted in Eq. (45) to express the regression in non-dimensional form $M/(\sigma_Y D_0 t)$, ensuring physical consistency across configurations.
Eq. (16-17)	Reference Resistance Design (RRD) incorporating partial resistance factors (ϕ, R_m).	Serves as a comparative reference for validating the regression predictions, Eqs. (43 - 45) against established design-based strength formulations.
Eq. (35-40)	Transversely isotropic bending formulation for composite or anisotropic shells.	Included as a contextual background, not applied directly in Eqs. (43 - 45) since the current study assumes isotropic metallic material.

4.9. Derived Formula

A forecasting formula was derived to predict the ultimate bending capacity of tapered shells based on 900 FEM results, with a normalization constant (0.875) introduced to align analytical and numerical predictions. In this formulation, L denotes the shell length [m], D_0 the bottom diameter [m], D_1 the top diameter [m], t representing wall thickness [m], σ_y representing material yield stress [MPa], and M the ultimate bending moment [kN.m]. The analysis further considers the dimensionless ratios ($\frac{L}{D_0}$), ($\frac{D_1}{D_0}$), and ($\frac{D_0}{t}$). Within the multiplicative forecasting framework, the regression coefficients a, b, c, and d were identified, and the resulting expression is presented in Equation (43).

$$\left(\frac{L}{D_0}\right)^b \left(\frac{D_1}{D_0}\right)^c \left(\frac{D_0}{t}\right)^d \left(\frac{\sigma_y \,.\, L^3}{0.875}\right) 10^a \;=\; M \tag{42}$$

The regression exponents a, b, and $c$in Equation (43) represent geometric sensitivity coefficients corresponding to slenderness (L/D_0), taper ratio (D_1/D_0), and diameter-to-thickness ratio (D_0/t). Their signs and magnitudes reflect the physical influence of these parameters on bending strength: higher slenderness and thinness reduce capacity, while larger taper ratios enhance it. These relationships are consistent with classical shell bending theories, confirming that the regression model preserves the underlying mechanics governing ultimate strength in tapered cylindrical shells.

Based on 900 data points, the regression analysis was conducted by varying the independent variable against the dependent variable, represented as the ultimate moment. Regression analysis yielded an R^2 and adjusted R^2 of 0.981, indicating that the cubic polynomial model accurately predicted the dependent variable with 98.1% accuracy. The cubic form was selected for its ability to capture the nonlinear relationship between variables, providing greater flexibility in representing the distributed data. The coefficient values for each variable were calculated and listed in Table 6. The forecasting formula can be seen in the following Equation (44).

Table 6. Regression analysis summary.

Constant	Unstandardized Coefficient			R^2	Adj. R^2
	$\frac{L}{D_0}$	$\frac{D_1}{D_0}$	$\frac{D_0}{t}$		
3.221	-2.999	1.694	-1.153	0.981	0.981

$$M = \left(\frac{L}{D_0}\right)^{-2.999}\left(\frac{D_1}{D_0}\right)^{1.694}\left(\frac{D_0}{t}\right)^{-1.153}\left(\frac{\sigma_y \,.\, L^3}{0.875}\right)10^{3.221} \tag{43}$$

The equation shows that all geometric parameters influence the ultimate strength of the tapered pipe, with the slenderness ratio being the primary determinant of structural capacity. The diameter and thickness ratios contribute secondarily but remain relevant to overall strength behavior. To maintain dimensional consistency, the combined term ($\sigma_y \,.\, L^3$) was normalized using a reference constant (0.875) with identical units, producing a dimensionless variable that improves numerical stability while preserving physical meaning. The multiplicative constant 10^e in Equations (43 - 44) represents the back-transformed intercept from the $\log_{10}$ regression and is therefore required to recover predictions on the original moment scale. This factor ensures dimensional consistency and preserves the physical scaling of the moment-geometry relationship. Its inclusion does not affect relative scaling across the studied geometrical domain, as verified through residual diagnostics, but extrapolation to extreme geometries beyond the calibrated range may lead to increased uncertainty. Dimensional consistency and parameter sensitivity were verified to ensure physically realistic predictions across the full geometric range.

4.10. Derived Formula Dimensional Check and Normalization

In Equation (44), the factor $\sigma_y L^3$ has units of moment $[F \cdot L]$ since $[\sigma_y] = [F/L^2]$ and $[L^3] = [L^3]$. All other multipliers and the geometric ratios are dimensionless, so M_u retains the correct units. For a section-based normalization with $M_p = \sigma_y D_0^2 t$, the same model becomes Equation (45).

$$\frac{M_u}{M_p} = C'\left(\frac{L}{D_0}\right)^{a+3}\left(\frac{D_1}{D_0}\right)^{b}\left(\frac{D_0}{t}\right)^{c+1} \tag{45}$$

where $C' = \frac{10^e}{0.875}$ which is the re-parameterization of the same model (no refit, no change in predictions).

4.11. Derived Formula Validation

The validation of Equation (7) was conducted by comparing the ultimate bending capacity obtained from numerical simulations with the predictions of the derived regression formula, as presented in Figure 29 and Tables 7–8. The results show a high level of agreement, with an average percentage difference of approximately 4.85% and most deviations remaining below 10%. This confirms that the proposed regression model accurately predicts the ultimate bending moment across various configurations and demonstrates strong consistency with the FEM database. The slight deviation between analytical and numerical results indicates that the derived formula effectively captures the nonlinear influence of taper geometry and material yield stress on the structural response. Minor discrepancies exceeding 10% were observed only when the taper ratio approached unity or when the wall thickness was excessive, leading to localized stiffness variations that are not fully represented by the regression parameters. Validation using additional geometric configurations beyond the regression set further verified the model's predictive capability.

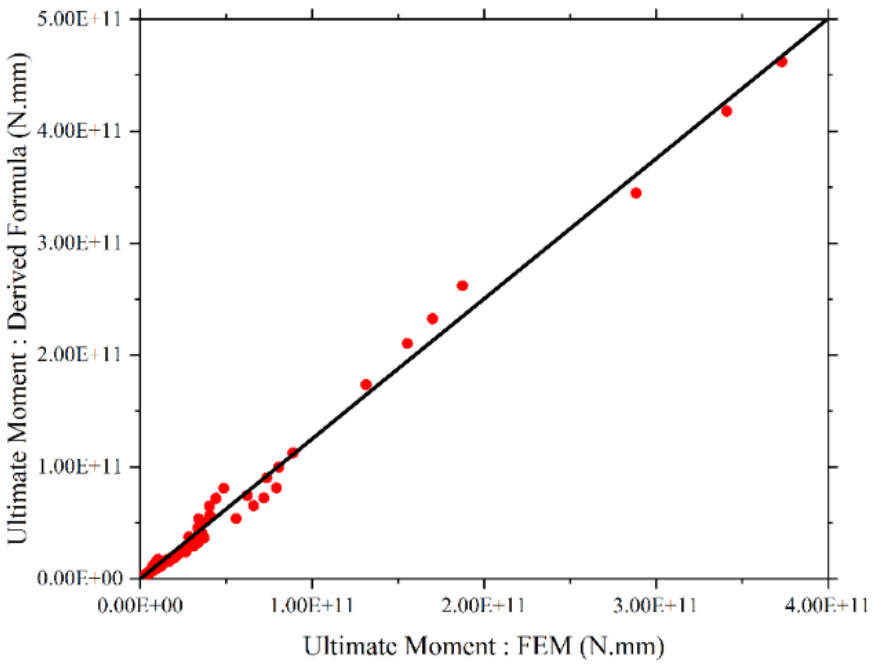

Figure 29. Comparison of the derived formula to FEM.

Table 7. Validation of the derived formula.

Length (m)	L/D_0	D_1/D_0	D_0/t	σ_y	Ultimate Moment (kN.m)		Difference (%)
					FEM	Derived Formula	
15	30	0.75	60	355	511.7	461.6	9.79
20	125	0.6	80	355	7.356	7.446	1.23
20	250	0.4	160	355	0.199	0.211	5.63
25	25	0.4	60	355	123.8	127.3	2.82
35	140	0.3	125	355	4.872	5.248	7.71
35	250	0.8	140	355	4.333	4.261	1.67
40	40	0.6	80	355	1981	1816	8.32
40	80	0.7	125	355	189.3	176.3	6.88
40	250	0.6	160	355	3.304	3.349	1.38
60	40	0.45	120	355	2433	2359	3.06
Average difference (%)							4.85

Table 8. Samples of variations outside the selected range in Equation (45).

Length (m)	L/D_0	D_1/D_0	D_0/t	σ_y	Ultimate Moment (kN.m)		Difference (%)
					FEM	Derived Formula	
10	20	1	10	355	5617.5	6782	20.72
10	100	0.75	10	355	25.7	33.3	29.87
10	300	0.25	10	355	0.27	0.19	29.73
30	20	1	10	355	152705	183113	19.91
30	200	0.5	10	355	44.52	56.7	27.35

30	300	1	50	355	6.63	8.49	28.05
50	20	0.5	10	355	187507	262022	39.74
50	100	1	200	355	185.25	214.39	15.73
50	200	0.75	10	355	396.47	521.68	31.58
50	400	1	100	355	6.38	7.46	16.89

$$M = \left(\frac{L}{D_0}\right)^{-2.999}\left(\frac{D_1}{D_0}\right)^{1.694}\left(\frac{D_0}{t}\right)^{-1.153}\left(\frac{\sigma_y \,.\, L^3}{0.875}\right)10^{3.221}\; for\; 0.3 \le \frac{D_1}{D_0} \le 0.8\; and \frac{D_0}{t} \ge 50 \qquad (44)$$

To ensure accurate predictions of the ultimate bending capacity, it is essential to define the practical limitations and provide recommendations for the application of the derived formula**.** Several models with variations in slenderness ratio and taper degree confirmed that the difference between FEM and analytical results remains below 10% within the valid range. However, higher deviations may occur at extreme geometries, emphasizing the importance of applying the formula within the recommended bounds of 0.3 $\le D_1/D_0 \le 0.8$ and $D_0/t \ge 50$. Although the regression was calibrated using 900 datasets to capture overall behavior, reliable use should remain within these limits to maintain accuracy and stability.

The findings of this study substantiate the hypothesis that the proposed regression model is statistically robust and practically viable within the recommended domain. However, it is imperative to acknowledge that beyond the geometric applicability limits, further methodological considerations must be recognized. The validation results demonstrate the consistency of the derived regression formula with finite element simulations and reference studies, exhibiting a maximum discrepancy of 5% in the majority of cases. The regression formula effectively captures the influence of geometric parameters and yield stress. This demonstrates that the proposed expression can reliably approximate the ultimate bending moment while significantly reducing computational demand compared to full-scale FE simulations. Concurrently, a series of simplifying assumptions were implemented, encompassing the utilization of an isotropic elastic plastic material model, pure bending loads, and clamped free boundary conditions, whilst disregarding the consideration of initial imperfections or combined loading. These assumptions were deliberately chosen to isolate the influence of taper ratio and shell slenderness while maintaining computational efficiency. Furthermore, although mesh sensitivity was observed for coarse discretization, a mesh convergence study confirmed that results converge and become insensitive once the mesh size reaches approximately 55 mm. Notwithstanding the aforementioned limitations, the present study contributes a validated and computationally efficient prediction tool, providing a solution to the lack of simple design-oriented formulas for tapered cylindrical shells under bending.

5. Conclusions

A comprehensive series of ultimate strength analyses of tapered pipes was performed by varying and cross-combining the pipe length, the length-to-bottom-diameter ratio, the upper-to-bottom diameter ratio, the bottom diameter-to-thickness ratio, and the yield strength of the material. The analyses were conducted using the finite element method. From these results, a novel regression-based empirical formula was explicitly developed for tapered pipes to predict their ultimate bending capacity, representing a new contribution that extends beyond existing prismatic shell theories.

- The shape of tapered pipes, with varying geometric parameters such as length, slenderness ratio, degree of taper, and thickness, significantly influences both the ultimate strength and the critical failure modes of the pipe when subjected to a bending load.
- The cubic polynomial formula offered a highly accurate model for predicting the ultimate strength of the model under bending load, as it can capture the nonlinear relationship between dependent and independent variables, offering more flexibility and value for analyzing diverse data in a broad range of conditions.
- The newly derived formula, obtained through regression analysis of 900 FEM cases, provides an efficient and reliable design tool that substantially reduces the time required to predict bending capacity compared with full numerical simulations.
- The formula is currently applicable to hollow tapered pipes within the calibrated geometric and material ranges, ensuring accurate and physically consistent results. Future work should focus on extending the formulation to include fabrication-related imperfections, residual stress effects, and

dynamic environmental loading, thereby broadening its applicability for practical offshore and wind-turbine tower designs.

This study thus introduces a geometry-sensitive and validated predictive formulation for tapered pipes, bridging the gap between classical analytical models and modern computational methods in offshore and wind-turbine structural design.

Author Contributions

Raden Althaaf Ulwandaffa Dhaneswara: Validation, Formal analysis, Investigation, Data Curation, Writing - Original Draft. Alfido Marchandi Faizatama: Visualization, Writing - Review & Editing. Hensa Akbar Al Kautsar: Visualization, Writing - Original Draft. Ristiyanto Adiputra: Conceptualization, Methodology, Investigation, Writing - Review & Editing, Supervision, Project administration, Funding acquisition. Aditya Rio Prabowo: Conceptualization, Investigation, Writing - Original Draft, Writing - Review & Editing, Supervision. Sören Ehlers: Conceptualization, Writing - Review & Editing. Moritz Braun: Conceptualization, Writing - Review & Editing. Bambang Kusharjanta: Writing - Original Draft, Supervision. Eko Prasetya Budiana: Writing - Original Draft, Visualization. All authors have read and agreed to the published version of the manuscript.

Funding

This research was supported by Riset dan Inovasi untuk Indonesia Maju (RIIM) Batch 4 of the National Research and Innovation Agency (BRIN) and the Indonesia Endowment Fund for Education Agency (LPDP). The authors gratefully acknowledge the support.

Data Availability Statement

The data presented in this study are available in the article.

Conflicts of Interest

The authors declare that they have no conflict of interest.

References

Adie, P. W., Adiputra, R., Prabowo, A. R., Erwandi, E., Muttaqie, T., Muhayat, N., & Huda, N. (2023). Assessment of the OTEC cold water pipe design under bending loading : A benchmarking and parametric study using fi nite element approach. *Journal of the Mechanical Behavior of Materials*, *32(1)*, 20220298. https://doi.org/10.1515/jmbm-2022-0298

Adiputra, R., Fauzi, F. N., Firdaus, N., Suyanto, E. M., Kasharjanto, A., Puryantini, N., Erwandi, E., Rasgianti, R., & Prabowo, A. R. (2023). Roundness and slenderness effects on the dynamic characteristics of spar-type floating offshore wind turbine. *Curved and Layered Structures, 10(1)*, 20220213. https://doi.org/10.1515/cls-2022-0213

Ahmed, F., Foley, A., Dowds, C., Johnston, B., & Al, D. (2024). Assessing the engineering, environmental and economic aspects of repowering onshore wind energy. *Energy*, *301*, 131759. https://doi.org/10.1016/j.energy.2024.131759

Al-Habaibeh, A., Manu, E., Clement, T., Shakmak, B., Selvam, J., & Lin, T.-H. (2025). Accelerating whole life carbon assessment in construction with artificial intelligence. *Energy Catalyst*, *1*, 54–67. https://doi.org/10.61552/ec.2025.004

Al Kautsar, H. A., Adiputra, R., Prabowo, A. R., Djordjevic, B., & Jurkovič, M. (2024). Structural integrity of tapered cylindrical shell: Study case of tower wind turbine. *E3S Web of Conferences*, *563*, 02033. https://doi.org/10.1051/e3sconf/202456302033

Beer, F. P., Johnston, E. R., DeWolf, J. T., & Mazurek, D. F. (2021). *Statics and Mechanics of Materials* (3rd ed.). McGraw-Hill.

Brazier, L. G. (1927). Flexure of Thin Cylindrical Shells. *Proceedings of the Royal Society of London. Series A, Containing Papers of A Mathematical and Physical Character*, *116*(773), 104–114. https://doi.org/10.1098/rspa.1927.0125

Brush, D. O., Almroth, B. O., & Hutchinson, J. W. (1975). Buckling of Bars, Plates, and Shells. *Journal of Applied Mechanics*, *42*(4), 911–911. https://doi.org/10.1115/1.3423755

Budisetyawan, D., Fauzi, F. N., Adiputra, R., Prabowo, A. R., Firdaus, N., Puryantini, N., Jurkovič, M., Susilo, D. D. & Widodo, P. J. (2025). Wind Turbine Reliability Forecast: A Technical Review on the Research Milestone and Assessment of the Energy Cost Using Monte Carlo Simulation. *Engineered Science 35*, 1502. https://dx.doi.org/10.30919/es1502

Chen, L., Franky, K., Zhang, H., & Xiong, X. (2023). Nonlinear stability analysis of high-strength steel cylindrical shells under global bending. *Structures*, *55*, 1320–1329. https://doi.org/10.1016/j.istruc.2023.06.081

Chen, X., Li, C., & Xu, J. (2015). Failure investigation on a coastal wind farm damaged by super typhoon: A forensic engineering study. *Journal of Wind Engineering and Industrial Aerodynamics*, *147*(2015), 132–142. https://doi.org/10.1016/j.jweia.2015.10.007

Chwalla, E. (1933). Pure bending of slender, thin-walled tubes with a straight axis. *ZAMM - Journal of Applied Mathematics and Mechanics*, *13*(1), 48–53. https://doi.org/10.1002/zamm.19330130108

Deng, R., Zhou, X., Ji, W., Li, R., Zheng, S., & Wang, Y. (2023). Coupled behaviour and strength prediction of tapered CFDST columns with large hollow ratios for wind turbine towers. *Engineering Structures*, *289*,

116287. https://doi.org/10.1016/j.engstruct.2023.116287
Dimopoulos, C. A., & Gantes, C. J. (2012). Experimental investigation of buckling of wind turbine tower cylindrical shells with opening and stiffening under bending. *Thin-Walled Structures*, *54*, 140–155. https://doi.org/10.1016/j.tws.2012.02.011
Doerich, C., & Rotter, J. M. (2011). Generalised capacity curves for stability and plasticity: Application and limitations. *Thin-Walled Structures*, 49(9), 1132–1140. https://doi.org/10.1016/j.tws.2011.04.005
Dvorak, M. J., Archer, C. L., & Jacobson, M. Z. (2010). California offshore wind energy potential. *Renewable Energy*, *35*, 1244–1254. https://doi.org/10.1016/j.renene.2009.11.022
Faizatama, A. M., Firdaus, N., Adiputra, R., Prabowo, A. R., Ghanbari-Ghazijahani, T., Fazeres-Ferradosa, T., Melnyk, O., & Salamena, G. G. (2025a). Hydrodynamic impact of cold-water pipes and mooring systems on KVLCC2 for floating OTEC platforms. *Ocean Engineering, 341*, 122491. https://doi.org/10.1016/j.oceaneng.2025.122491
Faizatama, A. M., Firdaus, N., Adiputra, R., Prabowo, A. R., Shame, B. H., Jurkovič, M., Purwoko, A. S., & Fil Ardi, A. M. T. (2025). Mooring stress analysis of oc3-hywind floating platform with variation anchor placement. *Structural Integrity and Life 25(2)*, 193-202. https://doi.org/10.69644/ivk-2025-02-0193
Fajuyigbe, A., & Brennan, F. (2022). A simplified formula for calculating the limit load of cracked offshore wind turbine monopile under bending. *Marine Structures*, *83*(April 2021), 103164. https://doi.org/10.1016/j.marstruc.2022.103164
Fauzi, F. N., Puryantini, N., Prabowo, A. R., Adiputra, R., Carvalho, H., Tjahjana, D. D. D. P., Firdaus, N., & Jurkovič, M. (2024). Implementation Assessment of the Offshore Wind Turbine (OWT) for Remote Regions' Electrification in Indonesia Based on Geographical Potential and Economic Attractiveness. *Engineered Science*, *32*, 1295. https://dx.doi.org/10.30919/es1295
Feliciano, J., Cortina, G., Spear, A., & Calaf, M. (2018). Generalized analytical displacement model for wind turbine towers under aerodynamic loading. *Journal of Wind Engineering & Industrial Aerodynamics*, *176*(September 2017), 120–130. https://doi.org/10.1016/j.jweia.2018.03.018
Gentils, T., Wang, L., & Kolios, A. (2017). Integrated structural optimisation of offshore wind turbine support structures based on finite element analysis and genetic algorithm. *Applied Energy*, *199*, 187–204. https://doi.org/10.1016/j.apenergy.2017.05.009
Hammad, A., & Yu, Z. (2024). A semi-analytical approach for dynamic responses of monopile-supported offshore wind turbines subjected to accidental loads. *Applied Ocean Research*, *153*(September), 104251. https://doi.org/10.1016/j.apor.2024.104251
Hegseth, J. M., & Bachynski, E. E. (2019). A semi-analytical frequency domain model for efficient design evaluation of spar floating wind turbines. *Marine Structures*, *64*(August 2018), 186–210. https://doi.org/10.1016/j.marstruc.2018.10.015
Hernandez-Estrada, E., Lastres-Danguillecourt, O., Robles-Ocampo, J. B., Lopez-Lopez, A., Sevilla-Camacho, P. Y., Perez-Sariñana, B. Y., & Dorrego-Portela, J. R. (2021). Considerations for the structural analysis and design of wind turbine towers: A review. *Renewable and Sustainable Energy Reviews*, *137*, 110447. https://doi.org/10.1016/j.rser.2020.110447
Hu, Y., Baniotopoulos, C., & Yang, J. (2014). Effect of internal stiffening rings and wall thickness on the structural response of steel wind turbine towers. *Engineering Structures*, *81*, 148–161. https://doi.org/10.1016/j.engstruct.2014.09.015
Huang, X., Li, B., Zhou, X., Wang, Y., & Zhu, R. (2022). Geometric optimisation analysis of Steel–Concrete hybrid wind turbine towers. *Structures*, *35*(July 2021), 1125–1137. https://doi.org/10.1016/j.istruc.2021.08.036
Iqbal, M., Adiputra, R., Rio, A., & Erwandi, E. (2023). Internal flow effects in OTEC cold water pipe: Finite element modelling in frequency and time domain approaches, Ocean Engineering, Vol.288 article no. 116056. https://doi.org/10.1016/j.oceaneng.2023.116056
Kim, D. K., Wong, A. M. K., Hwang, J., Li, S., & Cho, N. K. (2024). A novel formula for predicting the ultimate compressive strength of the cylindrically curved plates. *International Journal of Naval Architecture and Ocean Engineering*, *16*(2024), 100562. https://doi.org/10.1016/j.ijnaoe.2023.100562
Kim, J. H., Park, J. S., Lee, K. H., Kim, J. H., Kim, M. H., & Lee, J. M. (2014). Computational analysis and design formula development for the design of curved plates for ships and offshore structures. *Structural Engineering and Mechanics*, *49*(6), 705–726. https://doi.org/10.12989/sem.2014.49.6.705
Kyriakides, S., Ok, A., & Corona, E. (2008). Localization and propagation of curvature under pure bending in steel tubes with Lüders bands. *International Journal of Solids and Structures*, *45*, 3074–3087. https://doi.org/10.1016/j.ijsolstr.2008.01.013
Li, S., & Kim, D. K. (2022). Ultimate strength characteristics of unstiffened cylindrical shell in axial compression. *Ocean Engineering*, *243*, 110253. https://doi.org/10.1016/j.oceaneng.2021.110253
Liu, X., Lu, C., Li, G., Godbole, A., & Chen, Y. (2017). Tower load analysis of offshore wind turbines and the effects of aerodynamic damping. *Energy Procedia*, *105*, 373–378. https://doi.org/10.1016/j.egypro.2017.03.328
Mandal, P., & Redd, K. S. (2025). Techno-economic assessment of solar power tower and solar parabolic dish system in India. *Journal of Global Decarbonisation*, *Volume 2025*, *Numéro 1*, 1–17. https://doi.org/10.17184/eac.9496
Michael, E., Tjahjana, D. D. D. P., & Prabowo, A. R. (2021). Estimating the potential of wind energy resources using Weibull parameters: A case study of the coastline region of Dar es Salaam, Tanzania. *Open Engineering 11(1),* 1093-1104. https://doi.org/10.1515/eng-2021-0108
Mork, K. J., Spiten, J., Torselletti, E., Ness, O. B., & Verley, R. (1997). The SUPERB project & DNV'96: buckling

and collapse limit state. *Proceedings of the International Conference on Offshore Mechanics and Arctic Engineering (Offshore Technology)*, 79–89.
Park, J. S., Paik, J. K., & Seo, J. K. (2018). Numerical investigation and development of design formula for cylindrically curved plates on ships and offshore structures. *Thin-Walled Structures*, *132*(March), 93–110. https://doi.org/10.1016/j.tws.2018.08.009
Patil, N. A., Arvikar, S. A., Shahane, O. S., & Geetha Rajasekharan, S. (2023). Estimation of dynamic characteristics of a wind turbine blade. *Materials Today: Proceedings*, *72*, 340–349. https://doi.org/10.1016/j.matpr.2022.08.025
Polenta, V., Garvey, S. D., Chronopoulos, D., Long, A. C., & Morvan, H. P. (2015). Optimal internal pressurisation of cylindrical shells for maximising their critical bending load. *Thin-Walled Structures*, *87*, 133–138. https://doi.org/10.1016/j.tws.2014.11.012
Prabowoputra, D. M., & Prabowo, A. R. (2022). Effect of the phase-shift angle on the vertical axis Savonius wind turbine performance as a renewable-energy harvesting instrument. Energy Reports, 8, 57–66. https://doi.org/10.1016/j.egyr.2022.06.092
Prabowoputra, D. M., Hadi, S., Prabowo, A. R., & Sohn, J. M. (2020). Performance investigation of the savonius horizontal water turbine accounting for stage rotor design. *International Journal of Mechanical Engineering and Robotics Research*, Vol.9 (2), pp.184-189. https://doi.org/10.18178/ijmerr.9.2.184-189
Prasetyo, S. D., Prabowo, A. R., & Arifin, Z. (2022). Materials today : Proceedings The effect of collector design in increasing PVT performance : Current state and milestone. *Materials Today: Proceedings*, *63*, S1–S9. https://doi.org/10.1016/j.matpr.2021.12.356
Rehling, F., Delius, A., Ellerbrok, J., Farwig, N., & Peter, F. (2023). Wind turbines in managed forests partially displace common birds. *Journal of Environmental Management*, *328*(June 2022), 116968. https://doi.org/10.1016/j.jenvman.2022.116968
Ren, C., Aoues, Y., Lemosse, D., & Souza De Cursi, E. (2023). Reliability assessment of an offshore wind turbine jacket under one ultimate limit state considering stress concentration with active learning approaches. *Ocean Engineering*, *281*, 114657. https://doi.org/10.1016/j.oceaneng.2023.114657
Ren, W., Zhou, X. H., Deng, R., Wang, Y. H., & Cao, Y. Q. (2022). Experimental and analytical investigation of stiffened steel tubes for wind turbine towers under compression-bending load. *Journal of Constructional Steel Research*, *193*, 107296. https://doi.org/10.1016/j.jcsr.2022.107296
Rotter, J. M. (2005). Stability and plasticity in structural analysis: A new conceptual framework. *Proceedings of the Fourth International Conference on Advances in Steel Structures, Shanghai, China*. https://doi.org/10.1016/B978-008044637-0/50271-7.
Rotter, J. M. (2007). *A framework for exploiting different computational assessments in structural design*. In Proceedings of the Sixth International Conference on Steel and Aluminium Structures. Oxford, United Kingdom.
Rotter, J. M. (2011). Shell buckling design and assessment and the LBA-MNA methodology. *Stahlbau*, *80*(11), 791–803. https://doi.org/10.1002/stab.201101491
Rotter, J. M., Sadowski, A. J., & Chen, L. (2014). Nonlinear stability of thin elastic cylinders of different length under global bending. *International Journal of Solids and Structures*, *51*(15–16), 2826–2839. https://doi.org/10.1016/j.ijsolstr.2014.04.002
Rotter, J. M. (2016a). *Advances in understanding shell buckling phenomena and their characterisation for practical design.* In Proceedings of the XIII International Conference on Metal Structures. Zielona Góra, Poland.
Rotter, J. M. (2016b). *The new method of reference resistance design for shell structures*. In Proceedings of the International Colloquium on Stability and Ductility of Steel Structures. Timisoara, Romania.
Sadowski, A. J. (2019). On the advantages of hybrid beam-shell structural finite element models for the efficient analysis of metal wind turbine support towers. *Finite Elements in Analysis and Design*, *162*(May), 19–33. https://doi.org/10.1016/j.finel.2019.05.002
Sadowski, A. J., & Rotter, J. M. (2013). Solid or shell finite elements to model thick cylindrical tubes and shells under global bending. *International Journal of Mechanical Sciences*, *74*, 143–153. https://doi.org/10.1016/j.ijmecsci.2013.05.008
Shame, B. H., Haji, M. M., & Prasetyo, S. D. (2025). Implementation of rooftop solar photovoltaic systems in educational facilities at Ibu Kota Nusantara (IKN), *Mekanika: Majalah Ilmiah Mekanika*, Vol.24 (1) pp.20-34. https://doi.org/10.20961/mekanika.v24i1.92799
Som, P., & Deb, A. (2014). A generalized Ritz-based method for nonlinear buckling of thin cylindrical shells. *Thin-Walled Structures*, *76*, 14–27. https://doi.org/10.1016/j.tws.2013.09.024
Stephens, W. B., Starnes, J. H., & Almroth, B. O. (1975). Collapse of long cylindrical shells under combined bending and pressure loads. *AIAA Journal*, *13*(1), 20–25. https://doi.org/10.2514/3.49624
Sun, X., Huang, D., & Wu, G. (2012). The current state of offshore wind energy technology development. *Energy*, *41*(1), 298–312. https://doi.org/10.1016/j.energy.2012.02.054
Timoshenko, S. P., & Gere, J. M. (1985). *Theory of Elastic Stability* (2nd ed.). McGray-Hill.
Wang, J., Fajuyitan, O. K., Orabi, M. A., Rotter, J. M., & Sadowski, A. J. (2020). Cylindrical shells under uniform bending in the framework of Reference Resistance Design. *Journal of Constructional Steel Research*, *166*, 105920. https://doi.org/10.1016/j.jcsr.2019.105920
Wang, J., Qin, D., & Lim, T. C. (2010). Dynamic analysis of horizontal axis wind turbine by thin-walled beam theory. *Journal of Sound and Vibration*, *329*(17), 3565–3586. https://doi.org/10.1016/j.jsv.2010.03.011
Wijaya, M. R. A., Adiputra, R., Prabowo, A. R., Firdaus, N., Tjahjana, D. D. D. P., Carvalho, H., Smaradhana, D. F., & Fitri, S.N. (2025). Effect of designed stiffener configuration on natural frequency and buckling

behaviour of 5 MW NREL wind turbine blade structure using FE method. *Ship Technology Research 72(2)*, 99-119. https://doi.org/10.1080/09377255.2024.2437309

Xu, Y., Ren, Q., Zhang, H., & Shi, W. (2021). Collapse analysis of a wind turbine tower with initial-imperfection subjected to near-field ground motions. *Structures*, *29*, 373–382. https://doi.org/10.1016/j.istruc.2020.11.019

Yadav, K. K., & Gerasimidis, S. (2019). Instability of thin steel cylindrical shells under bending. *Thin-Walled Structures*, *137*, 151–166. https://doi.org/10.1016/j.tws.2018.12.043

Yanez-Rosales, P., Río-Gamero, B. Del, & Schallenberg-Rodríguez, J. (2024). Rationale for selecting the most suitable areas for offshore wind energy farms in isolated island systems. Case study: Canary Islands. *Energy*, *307*, 132589. https://doi.org/10.1016/j.energy.2024.132589

Yang, Q., Li, Y., Li, T., Zhou, X., Huang, G., & Lian, J. (2022). Statistical extrapolation methods and empirical formulae for estimating extreme loads on operating wind turbine towers. *Engineering Structures*, *267*(June), 114667. https://doi.org/10.1016/j.engstruct.2022.114667

Yu, Z., & Amdahl, J. (2023). A Rayleigh-Ritz solution for high order natural frequencies and eigenmodes of monopile supported offshore wind turbines considering tapered towers and soil pile interactions. *Marine Structures*, *92*, 103482. https://doi.org/10.1016/j.marstruc.2023.103482

Zhang, S., Xu, Q., & Riffat, S. (2025). Green Technology & Innovation Multi-objective optimization of environmental retrofits in eldercare buildings : A case study in Suzhou. *X*(X). https://doi.org/10.36922/gti.7807